National Library of Canada — Bibliothèque nationale du Canada

Canadian Theses Service — Service des thèses canadiennes

Ottawa, Canada
K1A 0N4

NOTICE

The quality of this microform is heavily dependent upon the quality of the original thesis submitted for microfilming. Every effort has been made to ensure the highest quality of reproduction possible.

If pages are missing, contact the university which granted the degree.

Some pages may have indistinct print especially if the original pages were typed with a poor typewriter ribbon or if the university sent us an inferior photocopy.

Reproduction in full or in part of this microform is governed by the Canadian Copyright Act, R.S.C. 1970, c. C-30, and subsequent amendments.

AVIS

La qualité de cette microforme dépend grandement de la qualité de la thèse soumise au microfilmage. Nous avons tout fait pour assurer une qualité supérieure de reproduction.

S'il manque des pages, veuillez communiquer avec l'université qui a conféré le grade.

La qualité d'impression de certaines pages peut laisser à désirer, surtout si les pages originales ont été dactylographiées à l'aide d'un ruban usé ou si l'université nous a fait parvenir une photocopie de qualité inférieure.

La reproduction, même partielle, de cette microforme est soumise à la Loi canadienne sur le droit d'auteur, SRC 1970, c. C-30, et ses amendements subséquents.

NL 339 (r 88/04) c

Canada

COMPUTER-AIDED CHARACTERIZATION OF SINGLE CRYSTALS OF GaAs AND $Pb_{1-x}Gd_{x}Te$

ROBERT LE VAN MAO

A Thesis

in

The Department

of

Electrical and Computer Engineering

Presented in Partial Fullfillment of the Requirements
for the degree of Master of Applied Science at
Concordia University
Montreal, Canada

September 1991

© ROBERT LE VAN MAO, 1991

National Library of Canada

Bibliothèque nationale du Canada

Canadian Theses Service

Service des thèses canadiennes

Ottawa, Canada
K1A 0N4

The author has granted an irrevocable non-exclusive licence allowing the National Library of Canada to reproduce, loan, distribute or sell copies of his/her thesis by any means and in any form or format, making this thesis available to interested persons.

L'auteur a accordé une licence irrévocable et non exclusive permettant à la Bibliothèque nationale du Canada de reproduire, prêter, distribuer ou vendre des copies de sa thèse de quelque manière et sous quelque forme que ce soit pour mettre des exemplaires de cette thèse à la disposition des personnes intéressées

The author retains ownership of the copyright in his/her thesis. Neither the thesis nor substantial extracts from it may be printed or otherwise reproduced without his/her permission.

L'auteur conserve la propriété du droit d'auteur qui protège sa thèse. Ni la thèse ni des extraits substantiels de celle-ci ne doivent être imprimés ou autrement reproduits sans son autorisation.

ISBN 0-315-73687-9

Canadä

ACKNOWLEDGEMENTS

The author would like to thank his thesis supervisor, Professor A. Lombos, for providing help, advice and moral support which all contribute to the success of the present research work.

I am also grateful for the precious help of Dr. T. Bretagnon, Dr A. Jean, Dr. P. Silvestre and Professor J. P. Dodelet. Likewise Thanks are due to Professor C. Fau and Professor M. Averous for allowing the use of the Hall effect setup at Universite des Sciences et Techniques du Languedoc (Montpellier, France).

TABLE OF CONTENTS

Page

CHAPTER 1 INTRODUCTION 1

CHAPTER 2 CHARACTERIZATION TECHNIQUES AND THE COMPUTERIZED MEASUREMENT SYSTEMS 5

2.1 Resistivity measurements 5

2.2 Hall-effect measurements 10

2.3 Current-voltage (I-V) measurements 12

2.4 Capacitance-voltage (C-V) measurements 13

2.5 Principle of Deep Level Transient Spectroscopy (DLTS) 14

2.6 Measurement systems 20

2.2.1 Setup for resistivity and Hall effect measurements ... 20

2.2.2 Setup for I-V and capacitive measurements 25

CHAPTER 3 PREPARATION AND CHARACTERIZATION OF SAMPLES OF $Pb_{1-x}Gd_xTe$ 29

3.1 Sample preparation 29

3.1.1 Bulk growth by Horizontal Bridgman Method 29

3.1.2 Fabrication of Hall device 36

3.2 Experimental results 37

3.2.1 Magnetic characterization of the samples by EPR . . . 37

3.2.2 Electrical characterization of the samples . . . 40

3.3 Discussion 45

CHAPTER 4 PREPARATION AND CHARACTERIZATION OF EPITAXIAL LAYERS OF GaAs 50

4.1 Sample preparation 51

4.1.1 Epitaxial growth by Close-Space Vapor Transport technique (CSVT) 51

4.1.2 Fabrication of Hall devices 54

4.1.3 Fabrication of Schottky devices 54

4.2 Experimental results 55

4.2.1 Hall-effect measurements 56

4.2.2 I-V measurements 56

4.2.3 C-V measurements 60

4.2.4 Electron traps characterization by Deep Level Transient Spectrocospy 63

4.3 Discussion 68

CHAPTER 5 CONCLUSION 74

REFERENCES 76

APPENDIX A 80

APPENDIX B 82

LIST OF FIGURES

Figure

2.1 Generalized Van der Pauw layout used in resistivity and Hall effect measurements 7

2.2 Layout of 6-contact configuration used in resistivity and Hall effect measurements 9

2.3 Energy band diagram of a metal n- type semiconductor under different reverse biasing voltages 17

2.4 Schematic diagram showing the evolution of the depletion region of a Schottky barrier after an electrical excitation 18

2.5 Schematic diagram showing the relation between the DLTS spectra and the transient for a temperature scan 21

2.6 Schematic diagram of the system used for resistivity and Hall effect measurements 22

2.7 Simplified flowchart of the computer program for resistivity and Hall measurements 24

2.8 Schematic diagram of the system used for DLTS measurements 26

2.8 Simplified flowchart of the computer program for DLTS measurements 27

3.1 Schematic diagram of the Bridgman furnace and its temperature profile 31

3.2 The growth of spurious crystals nucleated at the intersection of the solid-liquid interface with the crucible wall .... [illegible]

3.3 The phase diagram of PbTe is given in (a). (b) shows the phase diagram near stochiometry 34

3.4 EPR spectra of a PbGdTe sample with x = 1% 36

3.5 The variation of ΔH as function of the atomic percentage of gadolinium in the ternary compound PbGdTe 39

3.6 Resistivity of different samples as function of the temperature 41

3.7 Carrier density of samples M6, M7 and M11 as function of the temperature 42

3.3 Carrier mobility of different samples as function of the temperature 43

3.9 Comparison between calculated and measured mobilities at 4.2K of PbTe and top mobilities measured in PbGdTe as the function of electron concentration for the n- type sample 49

4.1 Schematic representation of the CSVT deposition system . 52

4.2 Comparison of electron mobilities in n- type GaAs grown from SI undoped source measured at 77K with W. Walukiewick [49] theoretical calculations for different compensation ratios 57

4.3 Forward semilog I-V plots given at different temperatures for an Al/Pd n- type GaAs Schottky diode 58

4.4 Plot of V_o versus KT/e 59

4.5 Variation of the ideality factor with temperature 61

4.6 $1/C^2$ plot as a function of applied voltage for different temperatures 62

4.7 DLTS spectra of GaAs grown by Bridgman technique (A) and GaAs epitaxial layer (B) deposited by CSVT at a temperature of 880°C 64

4.8 DLTS spectra of epitaxial layers grown at different substrate temperatures (a SI source was used) 66

4.9 DLTS spectra of epitaxial layers grown with different kinds of sources: SI undoped (A2), Si-doped (B) and Zn-doped (C) 67

4.10 Evolution of EL2 versus substrate temperature 69

4.11 Variation of the concentration of ELCS1 versus the carrier concentration for samples grown using different sources 71

4.12 Arrhenius plot of ELCS1 of two samples with a doping level of $2.2\times10^{15}cm^{-3}$ and 3.2×10^{16} cm^{-3} 73

B.1 Schematic diagram of the cryostat 83

CHAPTER 1

INTRODUCTION

Two classes of semiconductors have been synthesized and their electronic properties are studied at the Solid-State Device Laboratory of Concordia University: epitaxial layers of gallium arsenide (GaAs) deposited by the Close-Space Vapor Transport technique (CSVT) and $Pb_{1-x}Gd_xTe$, a Dilute Magnetic Semiconductor (DMS), grown by the Horizontal Bridgman method. The techniques and systems applied to the characterization of these materials constitute the main axis of this study.

Recent papers have shown the possibility of using CSVT technique to deposit semi-insulating GaAs epitaxial layers [1]. This makes CSVT very interesting since it is an efficient and cost-effective deposition method in producing GaAs epitaxial films. These layers could be qualified for electronic devices such as solar cells [2] and FETs [3]. It is well known that deep levels in GaAs affect the electrical properties of the material and consequently the performance of resulting devices. Therefore the characterization process of the bulk traps is an important mean to assess the quality of the semiconductor. In the case of the large band gap semiconductor GaAs (1.4 eV), most of the effort in this work is focused on the characterization of n-type GaAs layers

fabricated by CSVT. The main capacitive technique used for characterization is Deep Level Transient Spectroscopy (DLTS) [4]. Since DLTS requires a Schottky barrier height close or superior to 0.80 eV [5], the Schottky diodes are fabricated using an Al/Pd system. The performance of the resulting diode will be reported. Two main electron traps are observed, EL2 and ELCS1, in most of GaAs samples [6]. The native donor level EL2 is observed in bulk GaAs as well as GaAs epitaxial layers grown using vapor-phase techniques and its origin is widely discussed in different papers [7,13]. Meanwhile, the deep level ELCS1 seems to be specific to GaAs epitaxial layers deposited by CSVT and its origin has to be identified.

The ternary compounds DMS are a class of materials which has unique properties and they continue to attract scientific interest [14]. This type of DMS is formed by including a permanent magnetic ion from the rare-earths or transition metal family in a known host matrix of type II-VI, IV-VI or III-V. Studies of electronic transport properties of $Hg_{1-x}Fe_xSe$ for $300^{\circ}K > T > 4.2^{\circ}K$ (liquid helium temperature) reveal that observed electron mobilities are higher than calculated mobilities [15,16]. The calculations take into account the contributions of optical phonon, acoustical phonons and scattering mechanism by charged centers for the given ion and electron concentration. In order to explain the observed results, Wigner's hypothesis on the formation of periodic superlattice of ionized charges is put forward [17,18].

The hypothesis of formation of an electron crystal in a positive background due to coulomb repulsive forces was mentioned for the first time by Wigner in 1938 [18]. To date, the only evidence of the existence of 2D Wigner lattice is established for a monolayer of electrons on the surface of liquid helium [19]. However, the primary conditions for 3D space-ordering of electrons as stated by Wigner's hypothesis are reunited in compensate DMS such as $Hg_{1-x}Fe_xSe$. The ionization of the transition metal Fe, randomly distributed in the host lattice, introduces a low-lying resonant donor level above the conduction band. Thisionization, according to [15], is not extended to all donor ions since it is constrained by (screened) Coulomb interaction. This may lead to the formation of a superlattice of ionized donors. In the DMS $Pb_{1-x}Gd_xTe$, the rare earth magnetic ion Gd^{+3} may have the same role as the transition metal Fe^{+3} in $Hg_{1-x}Fe_xTe$. In this case, the effective electron mobility can be higher than the one allowed by classical theory. Abnormally high mobility is already reported for this DMS [20]. Consequently, the study of the electron transport properties of $Pb_{1-x}Gd_xTe$ at Concordia University is motivated by the possibility of validating the concept of Three Dimensional Superlattice for this particular class of DMS [21].

The present thesis aims to provide further experimental study of: (1) the two main electron traps EL2 and ELCS1 in GaAs layers and (2) on the transport properties of samples of $Pb_{1-x}Gd_xTe$, with various atomic percentage of gadolinium (as determined by Electron Paramagnetic

Resonance measurements (EPR)). In the case of $Pb_{1-x}Gd_{x}Te$, transport properties are measured using alternatively Hall effect setups at Concordia University and at Groupe d'Etudes des Semiconducteurs of the Université des Sciences et Technique du Languedoc (USTL) in Montpellier (France). The transport properties were measured in the temperature range from 300°K to 4.2°K. EPR measurements were done at the Laboratoire de Physico-chimie des Matériaux Solides of the same university. The bulk growth of semiconductor was done using the Bridgman furnace at the Solid-State Device Laboratory of Concordia University. In the following sections, single crystal growth techniques (Bridgman, CSVT), device fabrication (Hall device, Schottky diode), and characterization techniques (Hall effect, DLTS, I-V and C-V) are described with appropriate details. Experimental results for most significant samples will be discussed. The discussion on $Pb_{1-x}Gd_{x}Te$ will emphasize Wigner's hypothesis and on how it could explain the observed results.

CHAPTER 2

CHARACTERIZATION TECHNIQUES AND THE COMPUTERIZED MEASUREMENT SYSTEM

Hall effect measurements and Deep-Level Transient Spectroscopy (DLTS) are currently the most valuable tools for the characterization of semiconducting materials in the laboratory. Meanwhile, the analysis of I-V and C-V characteristics provides additional information on the electrical properties of the Schottky devices used for DLTS measurements. Since most of these techniques required fast data gathering, they are well suited for computerization. The various characterization techniques and the associated instruments used to measure the electrical properties of the semiconductors $Pb_{1-x}Gd_xTe$ and GaAs are briefly described in the following sections.

2.1 Resistivity measurements

The resistivity of an extrinsic semiconductor, where usually one type of carrier is present, depends on the carrier concentration and the conduction mode in the material [22]. For convenience, this resistivity for an n-type crystal with a carrier density n where n >> p can be expressed as follows:

$$\rho = (n\ e\ \mu)^{-1} \quad (2.1)$$

n is the charge carrier density, μ is the mobility of the majority carrier and e is the electric charge ($e = 1.602\ 10^{-19}$ C). Since the semiconducting sample from which the resistivity is measured will be used later for Hall effect measurements, the configuration of the ohmic contacts are consequently designed to be appropriate for both techniques. The Hall device usually needs with four or six electrical contacts [22].

The 4-contact configuration is applied when laminar samples or thin layers are involved. The resistivity of the sample is deduced from the potential drop between two contacts for a given specimen current. The layout of a 4-contact sample is shown in figure 2.1. The current I is supplied via two of the contacts, A and B, and the potential drop V is measured between the other two contacts, C and D. Assuming the conducting layer is of uniform thickness and the sample is homogeneous, the sheet resistivity ρ can be deduced from the resistance measurements as follows:

$$R_{AB,CD} = \frac{V_D - V_C}{I_{AB}}, \quad R_{BC,DA} = \frac{V_A - V_D}{I_{BC}}.$$

Van Der Pauw [23] has shown the following relation:

$$\exp\left(\frac{-\pi t_s R_{AB,CD}}{\rho}\right) + \exp\left(\frac{-\pi t_s R_{BC,DA}}{\rho}\right) = 1 \qquad (2.2)$$

where t_s is the thickness of the laminar-type sample.

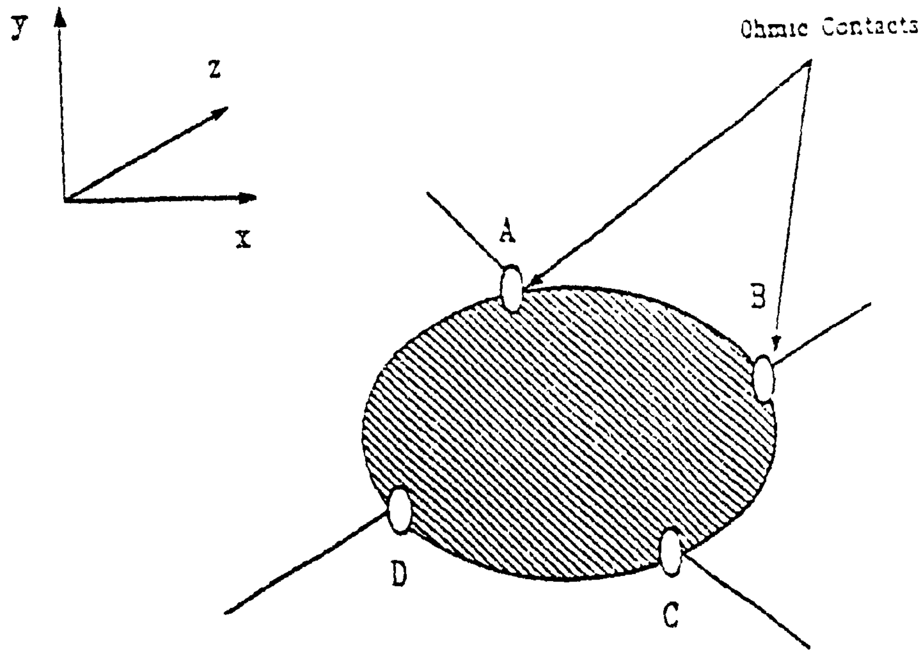

Figure 2.1 Generalized Van der Pauw layout used in resistivity and Hall effect measurements. The surface of the sample is parallel to the X-Y plane.

By developing equation (2.1) using equation (2.2), a complete expression for ρ as a function of the current I and of the measured voltage V can be deduced. It is given by [22]:

$$\rho = \frac{\pi}{8Ln(2)} \left[\frac{V_{CD}(+I_{AB})}{+I_{AB}} + \frac{V_{DA}(+I_{BC})}{+I_{BC}} + \frac{V_{CD}(-I_{AB})}{-I_{AB}} + \frac{V_{DA}(-I_{BC})}{-I_{BC}} + \frac{V_{AB}(+I_{CD})}{+I_{CD}} + \frac{V_{BC}(+I_{DA})}{+I_{DA}} + \frac{V_{AB}(-I_{CD})}{-I_{CD}} + \frac{V_{BC}(-I_{DA})}{-I_{DA}} \right] f t_s \quad \text{(Ohms.cm)} \qquad (2.3)$$

where f is a quality factor which value is pratically equal to 1. A complete expression for f is given by [22]. The sign indicates the direction of the current I.

In the case of a 6 contacts sample as shown in figure 2.2, the scenario to measure the voltage is simplified. When an electric current flows from E to F, the potential drops between the contacts A, B, C and D provide the data from which the resistivity of the sample is deduced. The average value of this resistivity is given by the following expression [22]:

$$\rho = \frac{1}{4} \left(\left[\frac{V_{AB}(+I)}{+I} + \frac{V_{AB}(+I)}{+I} \right] \frac{1}{d_{AB}} + \left[\frac{V_{DC}(-I)}{-I} + \frac{V_{DC}(-I)}{-I} \right] \frac{1}{d_{DC}} \right) w_s t_s \quad \text{(Ohms.cm)} \qquad (2.4)$$

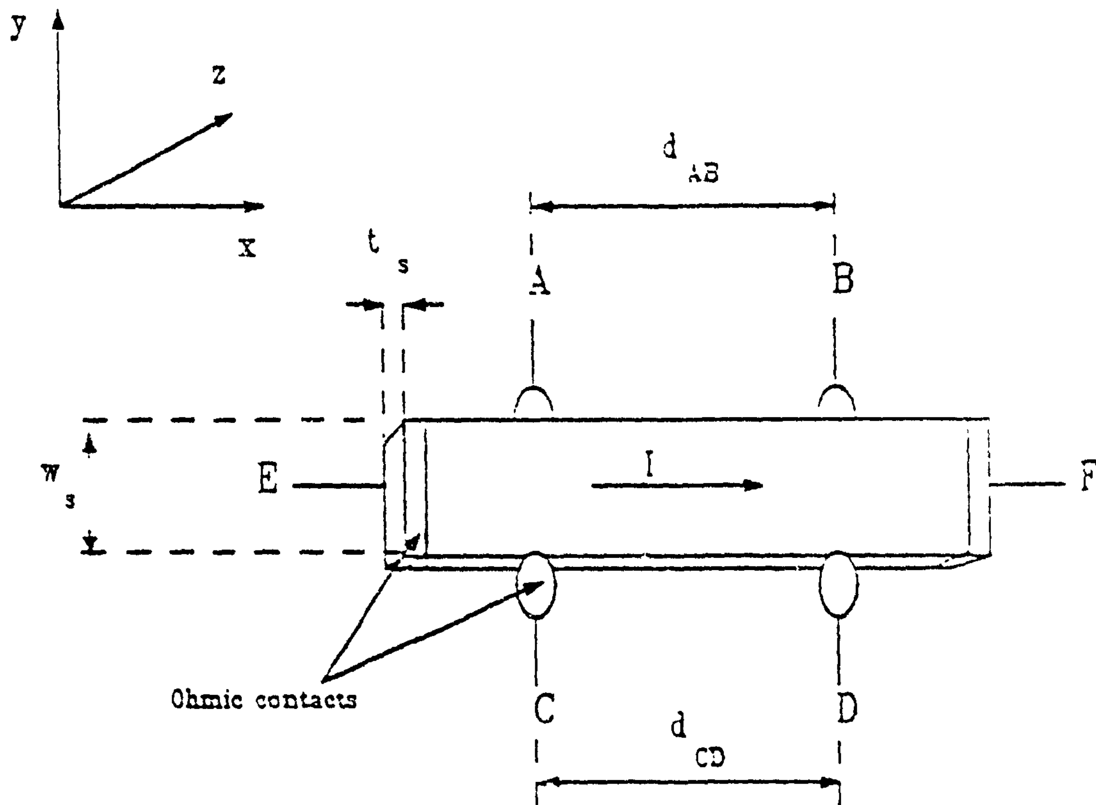

Figure 2.2 Layout of the 6-contact configuration used in resistivity and Hall effect measurements. The direction of the current I is parallel to the X-Y plane.

where d_{AB} is the distance between the contacts A and B, d_{DC} is the distance between the contacts D and C.

2.2 Hall-effect measurements

The Hall effect measurements provide a mean to determine the majority-carrier density and carrier mobility of the material under test. When a magnetic field B is applied, the free carriers travelling with a velocity v are subject to the Lorentz force e (B x v) and will be deflected in a direction perpendicular to the plane B and v. But since the current J inside a solid is constrained by its boundaries, the deflected electrons create a transverse electric field E which counterbalances the Lorentz force and enables the current to flow: this is the Hall electric field. For an n-type material with a carrier density n, its expression is given by (according to the coordinate system shown in figure 2.2):

$$E_y = - \frac{1}{n\,e} B_z\, J_x = - R_H\, B_z\, J_x \qquad (2.5)$$

where R_H is the Hall coefficient. In isothermal conditions, the Hall coefficient is then proportional to the gradient of the potential ($\partial V/\partial y$). For a 4-contact sample, the Hall coefficient R_H has the following expression [22]:

$$R_H = \frac{2.5 \times 10^7}{2} \left[\frac{V_{AC}(+I,+B)}{I_{BD}} + \frac{V_{AC}(-I,+B)}{-I_{BD}} - \frac{V_{AC}(-I,-B)}{-I_{BD}} - \frac{V_{AC}(+I,-B)}{+I_{BD}} \right.$$

$$\left. \frac{V_{BD}(+I,+B)}{I_{CA}} + \frac{V_{BD}(-I,+B)}{-I_{CA}} - \frac{V_{BD}(-I,-B)}{-I_{CA}} - \frac{V_{BD}(+I,-B)}{+I_{CA}} \right] \frac{t_s}{B}$$

$$(cm^3/C) \qquad (2.6)$$

In the case of a 6-contact sample, the expression of the Hall coefficient is given by [22]:

$$R_H = \frac{2.5 \times 10^7}{2} \left[\frac{V_{AD}(+I,+B)}{I} - \frac{V_{AD}(-I,+B)}{-I} - \frac{V_{AD}(-I,-B)}{-I} - \frac{V_{AD}(+I,-B)}{+I} \right.$$

$$\left. \frac{V_{BC}(+I,+B)}{I} + \frac{V_{BC}(-I,+B)}{-I} - \frac{V_{BC}(-I,-B)}{-I} - \frac{V_{BC}(+I,-B)}{+I} \right] \frac{t_s}{B}$$

$$(cm^3/C) \qquad (2.7)$$

In reality, the sample may not be homogeneous and a diffusion coefficient A is introduced in the expression of R_H ($= A\, n^{-1}\, e^{-1}$). However, the magnetic field is set such as $\mu B >> 1$ (in International System of Units) where μ is the Hall mobility, so this coefficient is reasonably assumed to be 1. Thus the carrier concentration can be obtained by:

$$n = \frac{1}{R_H e} \qquad (m^{-3}) \qquad (2.8)$$

The Hall mobility is defined as the ratio of the Hall coefficient to the resistivity measured at zero field:

$$\mu = \frac{R_H}{\rho} \qquad (m^{-2}.V^{-1}.s^{-1}) \qquad (2.9)$$

2.3 Current-voltage (I-V) measurements

For low-doped metal-semiconductor Schottky diodes, the dependence of the forward current I on the applied voltage V, according to the thermionic theory [24,25], is given as follows:

$$I = I_s \left(\exp\left(eV/(nkT)\right) - 1 \right) \qquad (2.10)$$

where k the Boltzmann's constant and T the absolute temperature. n is defined as the ideality factor of the diode. This is a dimensionless number introduced in order to take into account the deviation from ideality (n = 1 for a ideal Schottky barrier junction). I_s is the thermionic saturation current and its expression is given by [24]:

$$I_s = A^{*} T^2 S \exp\left(- e\phi_B/kT\right) \qquad (2.11)$$

where A^{*} is the modified Richardson's constant, S the area of the diode and ϕ_B the barrier height. In order to determine n and I_s, the current-voltage relationship can be described by the following equation [25,26]:

$$I = I_s \left(\exp \left(V/V_0 \right) - 1 \right) \qquad (2.12)$$

which reduces to $I = I_s (\exp (V/V_0))$ for the voltage range of $V/V_0 \geq 3$. In this case, the plot ln(I) versus V is a straight line whose the slope gives V_0 and the intercept with the voltage axis gives I_s. Then V_0 is plotted versus kT/e to verify whether the diode behaves as an Schottky barrier. If the diode has the behavior of an ideal Schottky diode then the plot V_0 versus kT/e will lead to a straight line with a slope equal to 1 (ie. n=1):

$$V_0 = \frac{kT}{e} \qquad (2.13)$$

Otherwise the value of n will be deduced and its dependency on the temperature could be investigated. According to equation (2.11), the Richardson plot I_s/T^2 versus 1/T should be a straight line whose slope gives the value of ϕ_B and the intercept on 1/T axis gives the value of A^*, the modified Richardson's constant.

2.4 Capacitance-voltage (C-V) measurements

The equivalent differential capacitance per unit area of a Schottky junction for an applied voltage V is given by [24]:

$$C = \frac{dQ}{dV} \qquad (F.cm^{-2}) \qquad (2.14)$$

where Q is the charge inside the space-charge region. For n-type material, this charge is due mainly to ionized donors. By solving the Poisson's equation for the space-charge region and by assuming a constant distribution of ionized donors, the following equation is obtained:

$$C = \left(\frac{e\, N_D\, \varepsilon}{2(V_{bi} + V)} \right)^{1/2} \qquad (2.15)$$

where V_{bi} is the built-in potential and N_D is the donors concentration. Then $N_d = N_D - N_A$ is deduced from the slope of the curve $1/C^2$ versus V and V_d from the intercept with the voltage axis.

2.5 Principle of Deep Level Transient Spectroscopy (DLTS)

The principle of DLTS is based on the study of the variation of the capacitance of a junction after an electric pulse at different temperatures [4]. This technique is used to characterize deep traps (located more than 100 meV away from the band limits) in the bulk semiconductor. From the study of the DLTS signal as a function of the temperature and the filling pulse width, one can deduce the activation energy E_T of the trap, its apparent capture cross-section and its density.

At thermodynamic equilibrium. the trap occupancy variation as a function of time for an n-type material is given by [27,28]:

$$\frac{dn_T}{dt} = -e_n n_T + nc_n(N_T - n_T) = 0 \qquad (2.16)$$

where n_T is the density of trapped electrons, N_T is the density of traps, e_n is the thermally-induced electrons emission rate, c_n is the electron capture rate, and n is the density of free electrons in the conduction band. The expression of n is given by [28]:

$$n = N_C \exp\left[- \frac{E_C - E_F}{KT} \right], \qquad (2.17)$$

where E_C is the energy of the conduction band edge, E_F is the Fermi energy, N_C is the density of states in the conduction band which is equal to $2M_C\left(\frac{2\pi m_{de} k}{h^2}\right)^{3/2} (T)^{3/2}$ (m_{de} is the density-of-state effective mass for electrons, M_C is the number of equivalent minima in the conduction band and h is Planck's constant). While the expression of c_n is given by [28]:

$$c_n = \sigma_n \bar{v}_n \qquad (2.18)$$

where σ_n is the electron capture cross section and $\bar{v}_n$ is the thermal velocity which is equal to $(3k/m^*)^{1/2}$ $(T)^{1/2}$ (m^* is the electron effective mass). The probability of the trap to be occupied, $f_T = n_T/N_T$, can be described by a Fermi function:

$$f_T = \left[1 + \frac{1}{g} \exp\left(\frac{E_T - E_F}{KT} \right) \right]^{-1} \qquad (2.19)$$

where g is the degeneracy factor and, in our case, is equal 1. Then according to equations (2.16) to (2.19), the emission rate is expressed as follows:

$$e_n = N_c \, c_n \exp\left[- \frac{E_c - E_T}{KT} \right] \qquad (2.20)$$

The Figure 2.3 shows a energy band diagram of a Schottky contact on an n-type material with a single donor level, which contributes to the depletion region, of length W_0, in the neighborhood of the metal-semiconductor interface. From this figure, a transition region of length λ can be distinguished as being the region where the Fermi level is still above the donor level. The mechanism of carrier injection to the deep electron trap in the depletion region of a Schottky barrier is shown in figure 2.4. An electrical impulse of opposite sign is superposed on the reverse bias voltage applied on the Schottky barrier. The resulting effect is the lowering of the deep donor level under the Fermi level, ie. the filling of these deep traps by majority carriers. The impulse must be long enough to allow all traps to fill: the study of the pulse width shall give then the apparent capture cross section of the trap. The impulse must be also high enough in order to fill all the traps in the depletion region: the assessment of the trap density and its profile can be done by varying the pulse height. The carrier emission out of the filled traps is thermally activated.

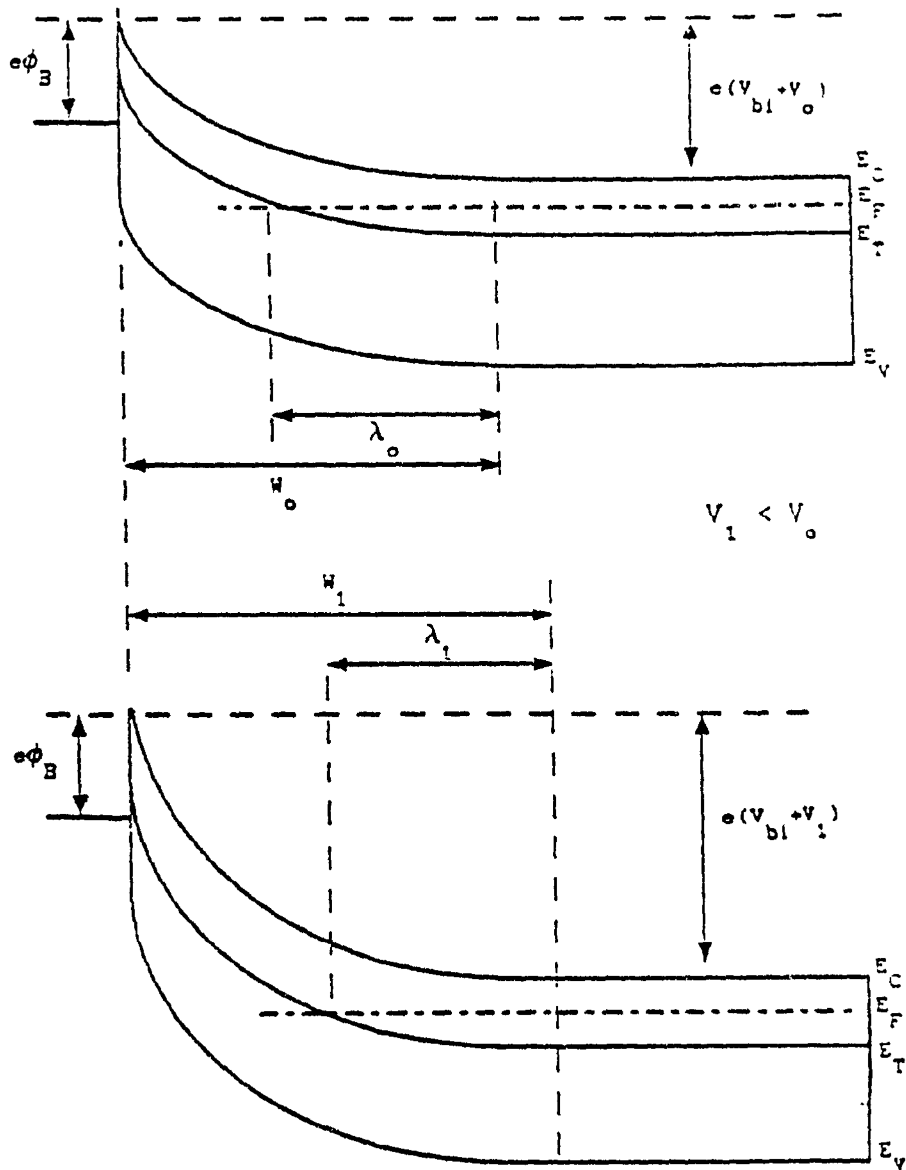

Figure 2.3 Energy band diagram of a metal n-type semiconductor under different reverse biasing voltages.

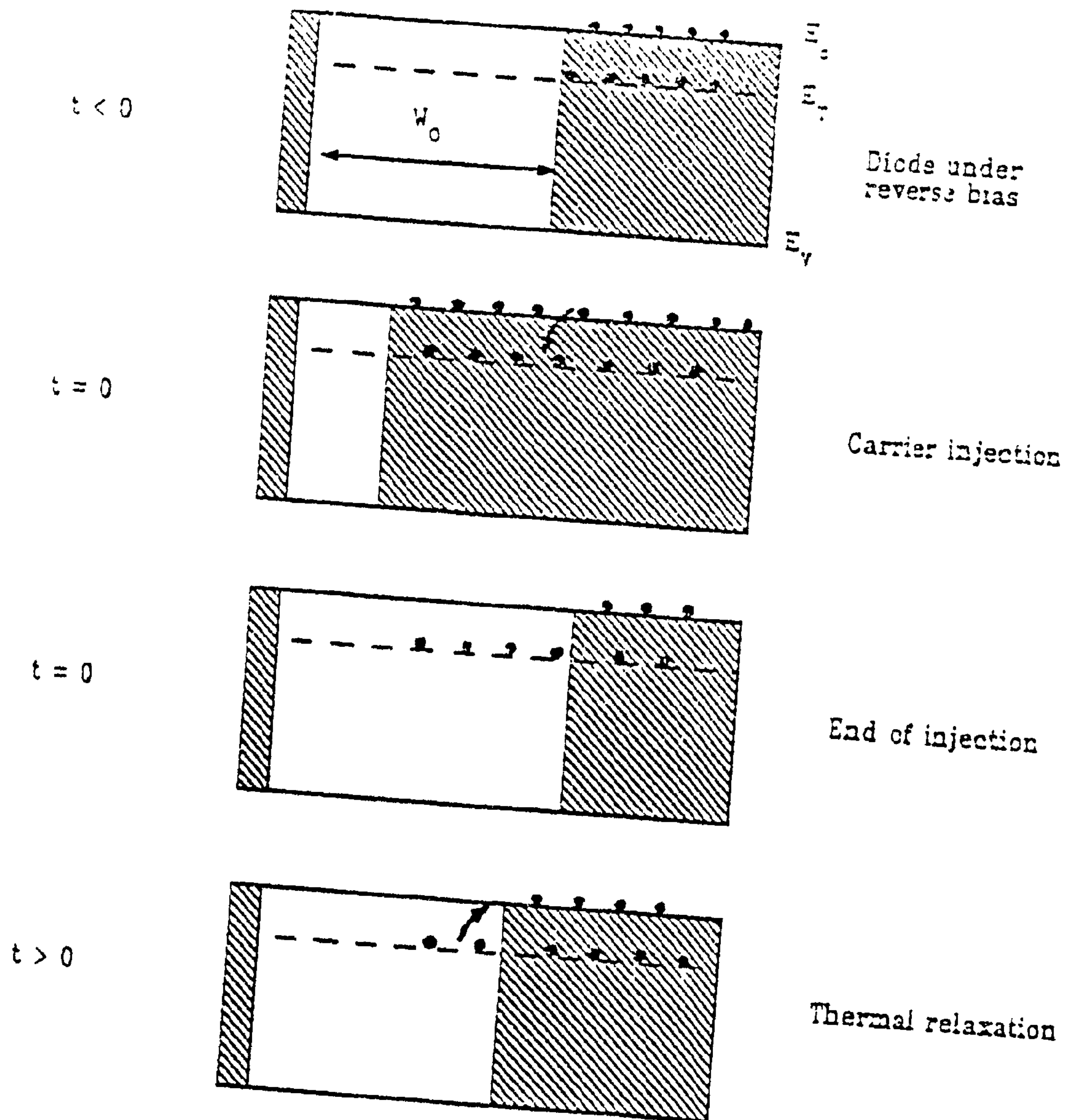

Figure 2.4 Schematic diagram showing the evolution of the depletion region of a Schottky barrier after an electrical excitation.

By considering the effect of the transition region, the following considerations are made: $n(x) << N_D - N_A$ for $x < W_0$, $\rho(x) = q(N_D - N_A)$ for $W_0 - \lambda < x < W_0$, and $\rho(x) = q(N_D - N_A + f_T N_T)$ for $0 < x < W_0$. $\rho(x)$ is the charge density and f_T is the filling factor of the deep level. By integrating the Poisson's equation for the transition region, λ is expressed as follows [29]:

$$\lambda = \left(\frac{2\epsilon}{e^2(N_D - N_A)} (E_F - E_T) \right)^{1/2} \qquad (2.21)$$

From the definition of a differential capacitance ($C = \epsilon S/W$) and considering $N_T << N_D$ (which is true in our case), the evolution of the capacitance is proportional to the evolution of the ionized deep-levels [29]:

$$\frac{\Delta C}{C} = \frac{C(t) - C_0}{C_0} = \frac{N_T}{2(N_D - N_A)} \frac{(W_1 - \lambda)^2 - (W_0 - \lambda)^2}{W_1^2} \qquad (2.22)$$

The analysis of this spectra is performed using the so-called Lang correlator [4]. The capacitive transient is recorded at different times t_1 and t_2 and can be expressed as follows [4]:

$$S_T(t) = \frac{C(t_1) - C(t_2)}{C_0}$$
$$= S_{To} \left[\exp(-e_n t_1) - \exp(-e_n t_2)\right] \qquad (2.23)$$

where e_n is the thermal emission rate of the trap. For the specif...

temperature T, this function has a maximum when:

$$e_n = \frac{\ln(t_2/t_1)}{t_2 - t_1} \qquad (2.24)$$

For each couple of (t_1, t_2), a specific value of e_n is computed and the corresponding value for T is deduced from the peak of the associated DLTS spectra. Figure 2.5 illustrates the relations between the DLTS spectra and the recorded transients. From the equations (2.17), (2.18), (2.20) and the expressions of N_c and $\bar{v}_n$, the Arrhenius plot of $\ln(T^2/e_n)$ versus 1/T will lead to a straight line in which the slope gives the ionization energy $E_A = E_C - E_T$ of the trap while its apparent capture cross section σ_n is deduced from the intercept with the axis for $1/T = 0$.

2.6 Measurement systems

2.6.1 Setup for resistivity and Hall effect measurements

The schematic diagram of the setup of the system used for Hall effect measurement is shown in figure 2.6. The setup includes a cryostat, an electromagnet (max. 1 tesla), a sweeptable water-cooled electromagnet controller from Walker Scientific Inc., a current generator Keithley 225, a scanner Keithley 706, a gaussmeter model 3265 from RFL Industries Inc., a multimeter HP-3455A and a computer HP-9153 series 300. Data transfer between the computer, the scanner and the multimeter is done though HPIB bus. The scanner Keithley 706 remotely

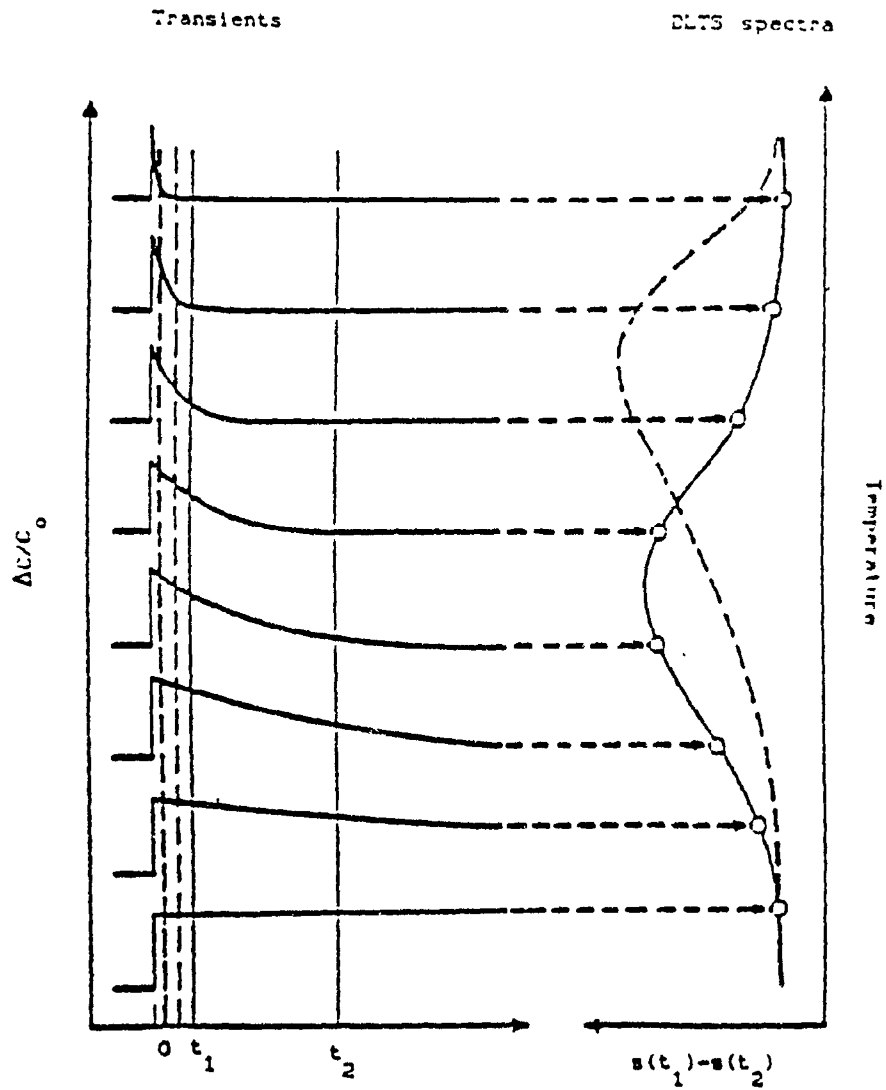

Figure 2.5 Schematic diagram showing the relation between the DLTS spectra and the transient for a temperature scan.

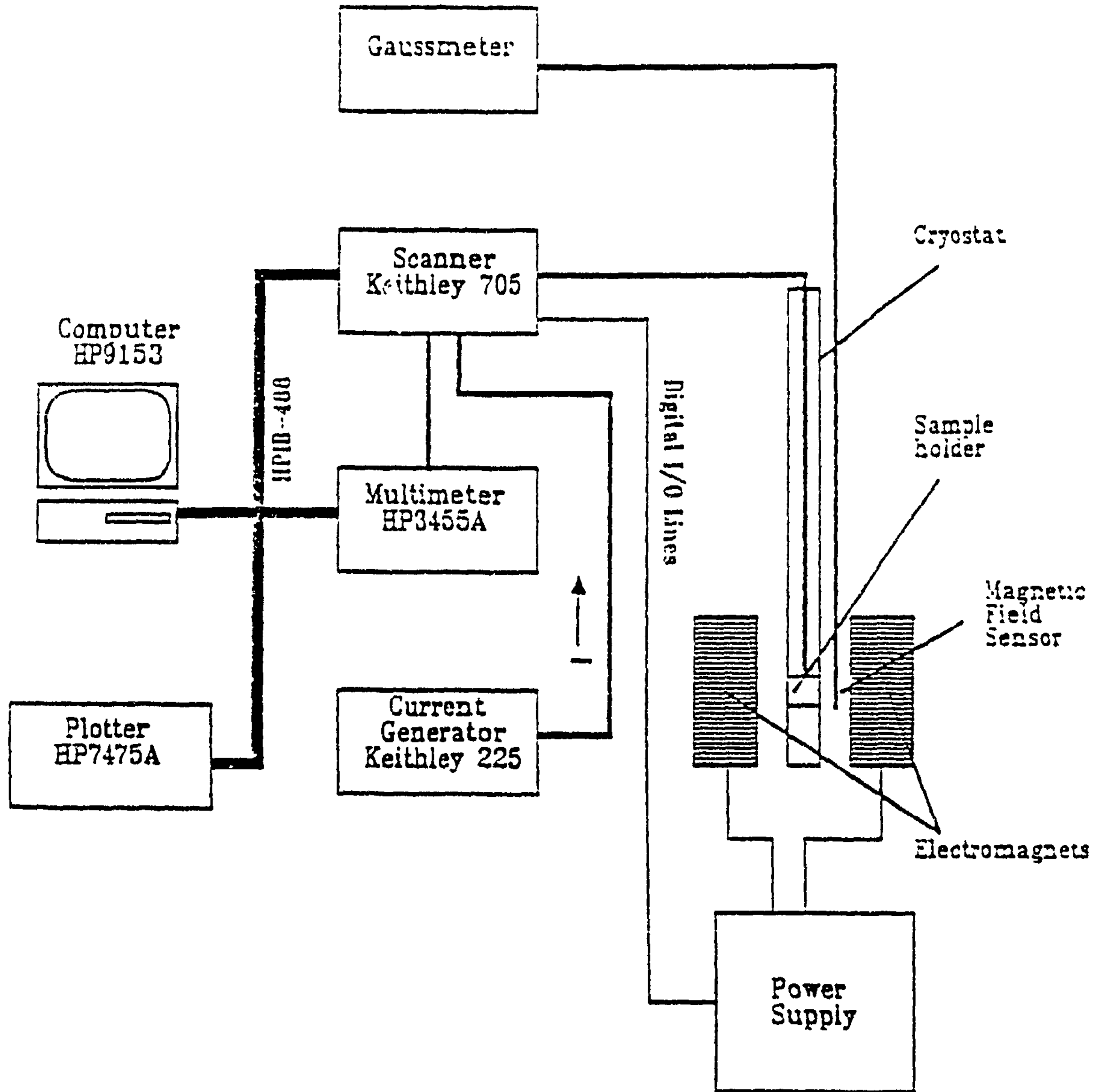

Figure 2.6 Schematic diagram of the system used for resistivity and Hall effect measurements.

commands the electromagnet controller though its digital I/O ... andserves as switching box. Its multichannel and matrix cards ... automatic reconfiguration of the system for I-V measurement, resist... and Hall effect measurements for 4-contact or 6-contact samples ... sample is fixed to the sample holder by silica grease, gold wires ... used to bond the contacts of the sample to the sample holder.

A simplified flowchart of the computer program developed ... collaboration with USTL is shown in figure 2.7. After having sel... the Hall effect measurements from the main menu, the user has to ent... details on the sample (4-contact or 6-contact type, thickness, etc. ... using the setup key. Prior to the beginning of the measurement cycle, the specimen current is manually set in the range from 10 μA to 10 mA as well as the magnetic field which is usually set to equal 5000 gauss (0.5 tesla). At first the computer will initialize the scanner according to the contact configuration of the sample, then it will measure the resistivity of the sample at zero field followed by the measurement of the Hall voltages at fixed magnetic field. The activation and shut down of the magnetic field and the switching of the current are do... automatically. The data are read from the multimeter and collected ... display or future analysis. The field is monitored by the gaussmeter and the temperature by a platinum resistance mounted on the sample holder

The Hall effect setup at the USTL were used for low-temperature measurements performed for samples of $Pb_{1-x}Gd_xTe$. Excepting the

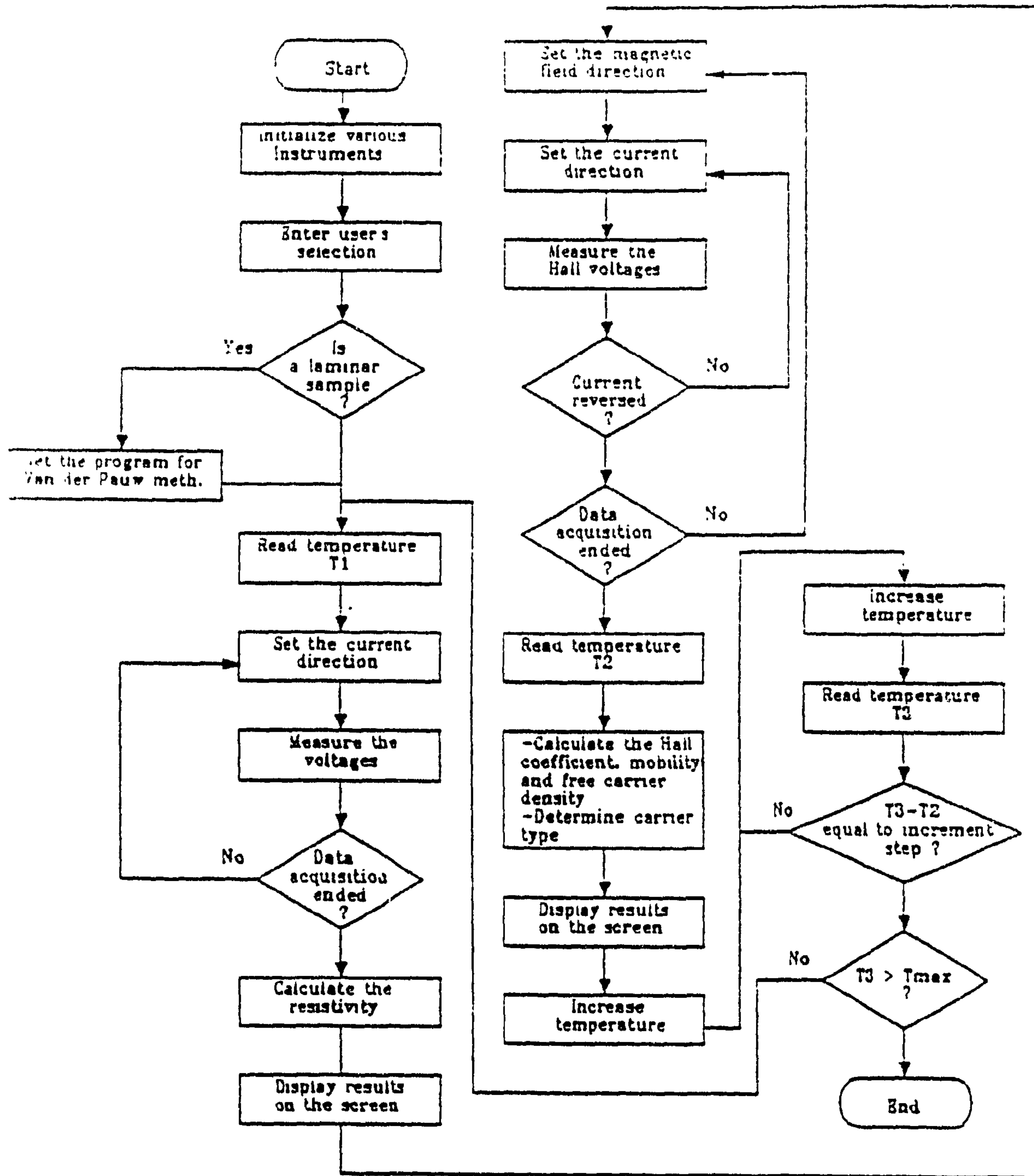

Figure 2.7 Simplified flowchart of the computer program for resistivity and Hall effect measurements.

cryostat, the data acquisition system a has similar design. It [illegible] a current generator Keithley 225, a scanner HP-3495A, a mult[illegible] HP-3490A and a computer Amstrad PC-1512. The last three commu[illegible] witheach other though an HPIB bus. The software running on the [illegible] follows the same algorithm as the one running on the HP-300 [illegible] initiates the measurement cycle described previously for [illegible] temperature increment until the specified maximum temperature. The [illegible] for each cycle are stored on disk as soon as they are collected.

2.5.2 Setup for I-V and capacitive measurements

The DLTS setup includes a capacitance meter HP-4280A, a pulse generator HP-8116A and a multimeter HP-3455A. These instruments are connected to the computer HP-9153 series 300 via an HPIB bus. The schematic diagram of this setup is shown in figure 2.8. The temperature is monitored by a platinum resistance and can be raised using a heater installed on the sample holder. Prior to the DLTS cycle, the same setup is used to obtain the I-V and C-V characteristics of the Schottky diode under test. These data provide important information on the device under test and which will be used in the DLTS analysis.

The DLTS cycle is controlled by the HP-9153 series 300. A flowchart of the program is shown in figure 2.9. At first, the temperature inside the cryostat is lowered down to the one of liquid nitrogen. For each temperature, the computer starts the data acquisition cycle on the

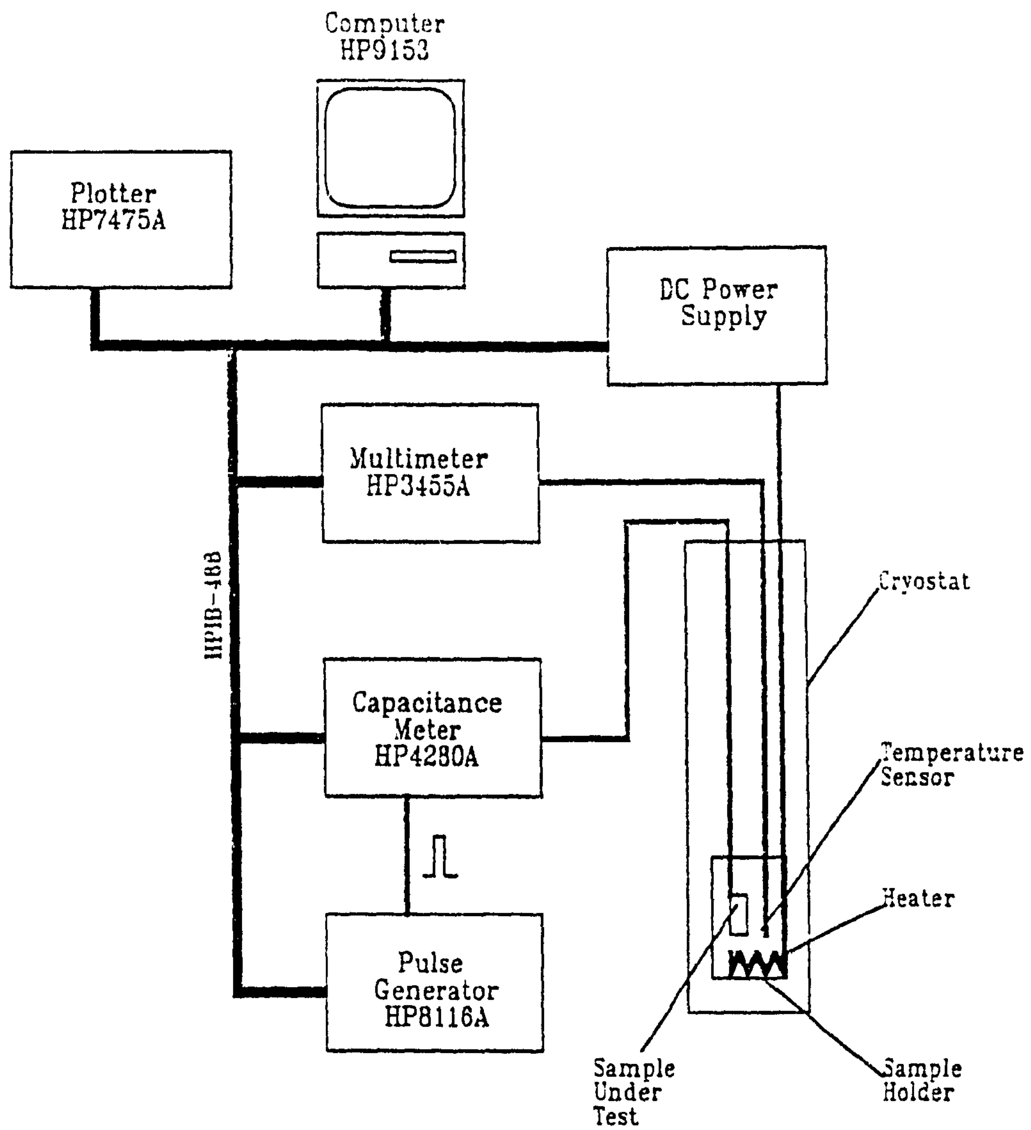

Figure 2.8 Schematic diagram of the system used for DLTS measurements.

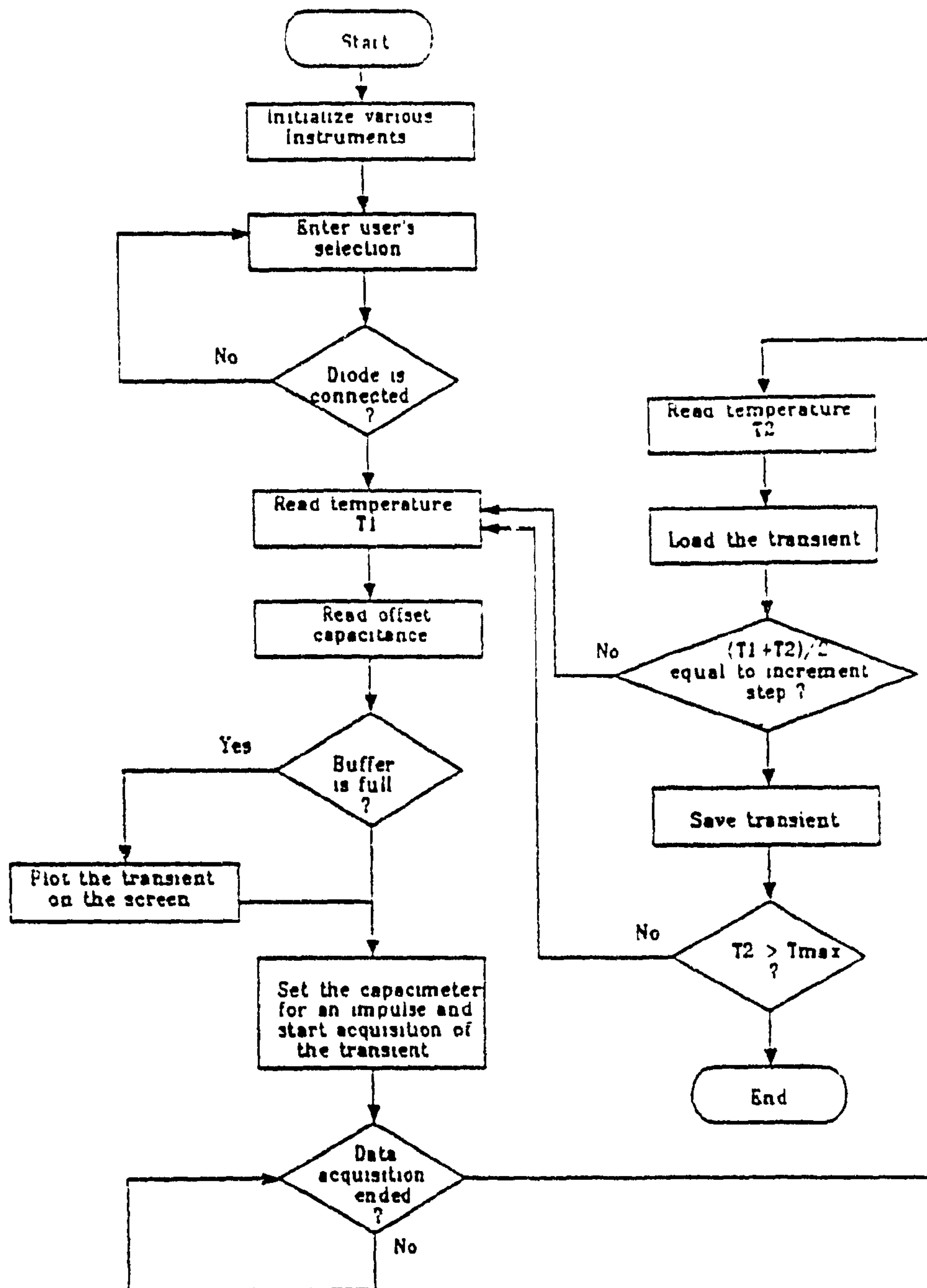

Figure 2.9 Simplified flowchart of the computer program for DLTS measurements.

capacitance meter, which in its turn triggers the pulse generator. The Schottky diode, which is under reverse bias, receives an electrical excitation of opposite sign which fills the traps in the space charge region with majority carriers. This will induce a lowering of the capacitance of the diode. When the electrical pulse ends, the capacitance of the diode is increasing exponentially since the traps are emitting the captured carriers. During this period, the capacitance meter is acquiring the data into its internal buffer memory. The number of points and the sampling rate, typically 50 Hz, can be remotely fixed from the computer.

When the recording of the transient is terminated, the gathered data are sent to the HPIB bus and stored by the computer for future analyses. The temperature swept from the beginning to the end of the data gathering cycle is about 1 ^{o}K/min. Finally, the temperature of the sample is raised to the next designated point in the experimental range and the measurement process is resumed by the program. The plotting of the Arrhenius curve as well as the calculation of the ionization energy of the deep traps and its apparent capture cross section are done by an analysis program (the original version was written at USTL).

CHAPTER 3

PREPARATION AND CHARACTERIZATION OF SAMPLES OF $PB_{1-x}GD_{x}TE$

$Pb_{1-x}Gd_{x}Te$ is a IV-VI semiconductor with a rare earth element Gd in substitutional position of lead in the host lattice. X ray studies [30] show a crystallization in a cubic face centered system like the one of NaCl. The average lattice parameter a (6.45 Å) is similar to the one of PbTe. To our knowledge, the band gap structure of $Pb_{1-x}Gd_{x}Te$ is not fully studied by experimental means. Significant changes in the energy gap can result from the replacement of lead by Gd^{+3} in PbTe. However, for small concentration of gadolinium, the band gap of $Pb_{1-x}Gd_{x}Te$ is practically identical to the one of PbTe (a direct gap with a minimum of 0.3 eV at the edge of the Brillouin zone (L)). In this study, the Horizontal Bridgman method is used to grow bulk crystals of $Pb_{1-x}Gd_{x}Te$. The method of preparation and results of transport properties measurements are reported in the following sections.

3.1 Sample preparation

3.1.1 Bulk growth by the Horizontal Bridgman method

The Bridgman growth method has been used to produce various DMS bulks crystals [31]. The principle of Bridgman growth is one of high

temperature directional growth from a melted solution. The melted and solidified materials are located in the same silica (or graphite) crucible with one end sharpened to favor nucleation.

A three-zone furnace mounted in a mobile platform is used for this experiment. The set up for the furnace and the temperature profile are shown in figure 3.1. A step motor provides the pulling action to the system through a gear assembly and its speed is adjusted by a stepping motor controller. The thermal transient is induced by the difference of temperature between the three zones. It covers practically the central zone. The gradient of this transient is varied using a Barber Colman temperature controller.

During the growth process, the melted material is slowly solidified by displacing the solid-liquid interface, induced by an appropriate thermal transient, along the growth axis. If the cold end of the crucible is correctly tapered, a single nucleation center is allowed to develop which leads to the formation of a single crystal. The displacement of the solid-liquid interface can be either vertical or, as in our case, horizontal. The advantage of a horizontal system is that only part of the interface is in contact of the interior of the crucible. In fact, random irregularities of the surface of the crucible may behave like undesired nucleation centers which may lead to the growth of polycrystals. This problem may be minimized by increasing the diameter of the crucible or by making the interface solid-liquid convex

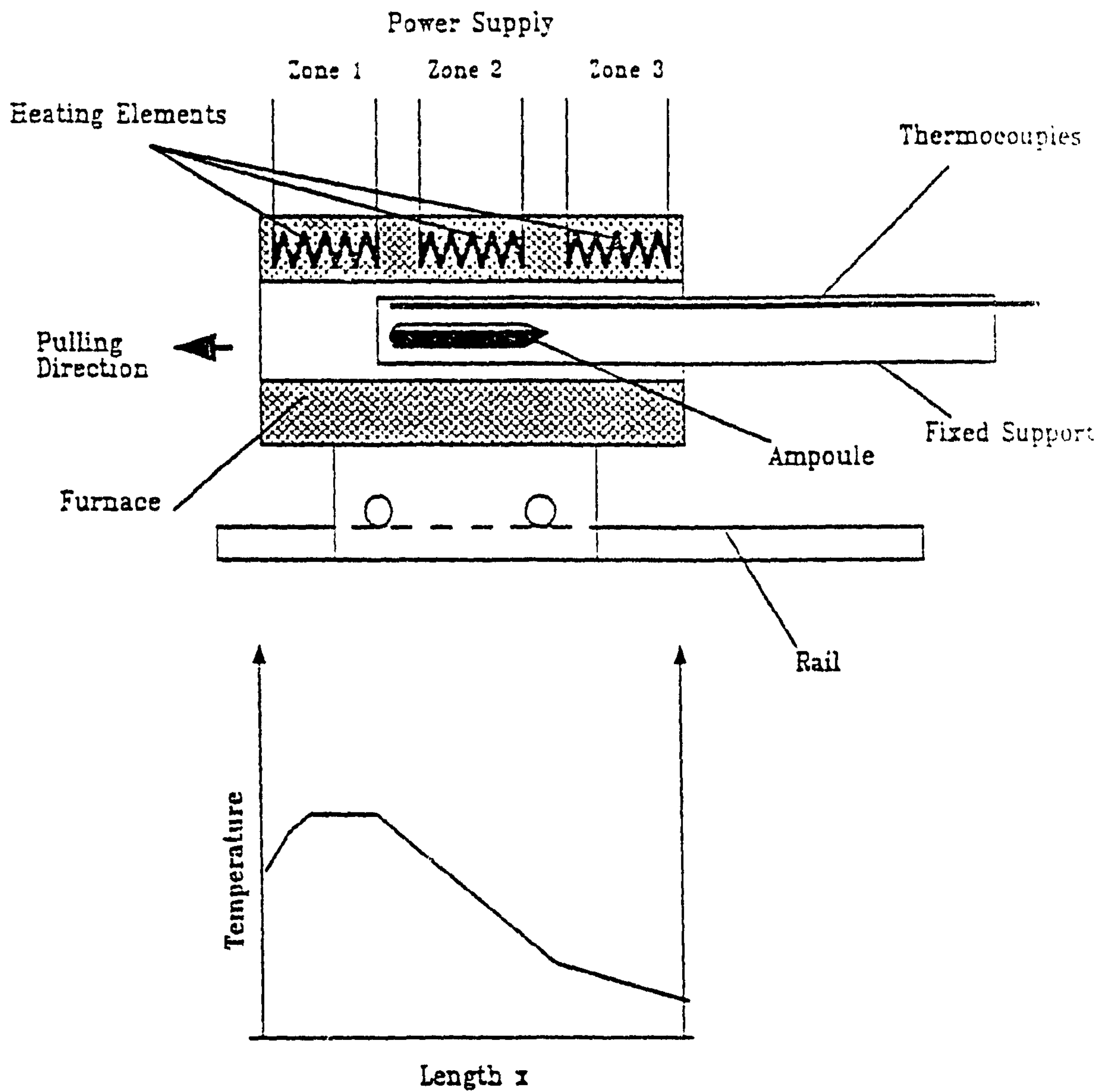

Figure 3.1 Schematic diagram of the Bridgman furnace and its temperature profile.

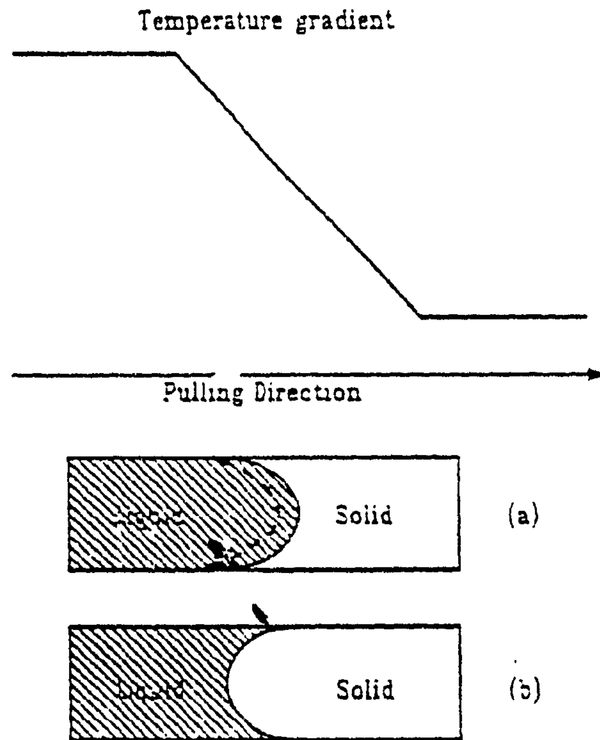

Figure 3.2 The growth of spurious crystals nucleated at the intersection of the solid–liquid interface with the crucible wall.

(a) Concave interface, stray crystal can grow in.
(b) Convex interface, any crystals nucleated are crowded out by the main crystal.

to the liquid side as shown in figure 3.2. In order to obtain the [illegible] shape for the interface, the crucible wall must have a higher temperature than its content. In our case, this can be achieved by using a fused silica crucible which has a good infrared transmission. The phase diagram of the binary compound lead telluride is given by [illegible] [32] and shown in figure 3.3. Since Te vacancies are doubly ionized donors [33], a deviation from stoichiometry is associated with the carrier type and density. This deviation is induced by the difference in atomic percentage between Te with respect to Pb. An excess of Pb leads to a n-type semiconductor. And vice-versa, an excess of Te leads to p-type semiconductor.

A fused silica ampoule containing the material has an internal diameter of around 12 mm. Prior to the introduction of the elements of electronic grade, the ampoule was degreased with hot trichloroethane, acetone and methanol. Then etched with a solution of HNO_3.HF.[illegible] (1:1:10), rinsed in distilled water and let dried in an oven at 80° C for about 12 hours. The elements, in fine granular format, have 5N (99.99999 % i.e. semiconductor grade) qualities and their atomic percentage are carefully measured in order to control the slight deviation from stoichiometric composition. The weight of each element, given the total weight of the charge W and the atomic percentage x of Gd, is calculated using the following formulas:

$$W_{Pb} = W\ (1 - x)\ m_{Pb}\ /\ M \qquad (gm) \qquad (3.1)$$

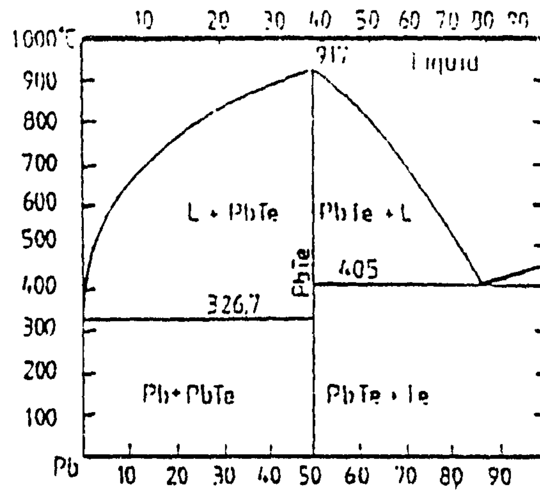

(a)

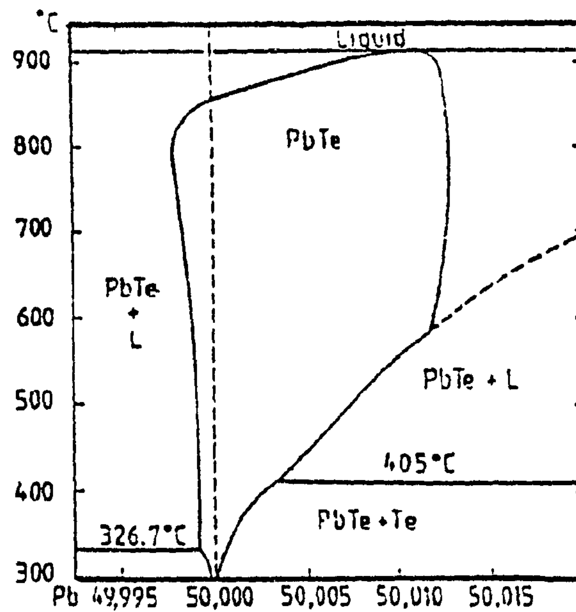

(b)

Figure 3.3 The phase diagram of PbTe is given in (a). (b) shows the phase diagram near stochiometry.

$$W_{Gd} = W\,(x)\; m_{Gd} \,/\, M \qquad (gm) \qquad (3.2)$$

$$W_{Te} = W\, m_{Te} \,/\, M \qquad (gm) \qquad (3.3)$$

Where m_{Pb}, m_{Gd}, m_{Te} and M are repectively the atomic weight of Pb, Gd, Te and the total of the weigth of each element. The expression for M is: $M = ((1-x)\, m_{Pb} + (x)\, m_{Gd} + m_{Te})$.

Once the elements are introduced, tne ampoule is sealed under a vacuum of 10^{-5} Torr and is brought to 950°C in the hottest zone of the furnace. It is then left at that temperature for 12 hours in order to allow the melted solution to homogenize. Then, by slowly moving the furnace, the ampoule is exposed to the cold region of the furnace. The crystal starts to form from the cold end of the ampoule where the temperature is below the temperature of fusion of the compound.

Since the crystal is grown from an intentionally doped solution, the pulling rate v is limited by the phenomenon of spurious nucleation [34]. This phenomenon is related to the diffusion of doping elements from the interface (Fick's law) and the rejection of these elements to the interface by solidification. In stationary situation, this limit is proportional to the temperature transient $(\frac{dT}{dx})$, the density of the doping elements in the liquid C_o and their diffusion coefficient in the liquid D_L:

$$v_{max} \propto \frac{C_o}{D_L} \left(\frac{dT}{dx}\right) \qquad (3.4)$$

As for our setup, satisfactory results are obtained with a pulling rate around 4.5 mm/hour and a gradient of temperature around 15° $C.cm^{-1}$. Once the ampoule is located entirely in the cold end of the furnace, the temperature of the furnace is dropped gradually until room temperature at a rate about 100°C/hour. Thereby the crystal is cooled very slowly. This prevents thermal shock which can lead to the formation of crystallographic defects in the bulk.

3.1.2 Fabrication of Hall device

The samples are cut from the bulk crystal into a parallepiped shape by a mechanical saw. Special care was accorded to the selection of the region from which the samples are cut since the polycrystalline regions or grain boundaries (made visible by iodine etching) are to be avoided. The configuration of the ohmic contacts has 6 points and is given by the ASTM F76-84 [22]. The ohmic contacts are obtained by electrolytic deposition of gold. The procedure for the fabrication of the ohmic contacts is provided in appendix A. A low emf alloy is used to solder the golden wires to the sample. The dimension of the specimen is around 5 cm in length, 1 to 2 cm width and 1 cm thick. I-V measurements reveal that the contacts are ohmics for the temperature range of 300°K to 4.2^{o}K.

3.2 Experimental results

3.2.1 Magnetic characterization of samples by EPR

The magnetic characterization of the samples is done in order to determine the effective atomic percentage x of magnetic ions Gd^{+3} in the sample of $Pb_{1-x}Gd_xTe$. Details on the principle of the EPR and the experimental set-up can be found in [30]. EPR measurements are performed at the USTL. The set-up available can detect from 10^{12} spins (or 10^{15} cm^{-3} for a volume of 1 mm^3). In our case, polycrystalline samples are taken at the vicinity of the region of the bulk where the samples used for transport measurements are cut. They are reduced in fine granular form before being put in the sample holder. The typical EPR spectra is shown in figure 3.4. The dissymetry of the signal is due to the dispersion distorsions [35]. From the spectra, the width ΔH at half amplitude of the resonant line can be determined. The obtained result is reported to a reference curve ΔH vs. x, as shown in figure 3.5, previously established for the compound $Pb_{1-x}Gd_xTe$.

Five significant n-type samples with different atomic percentages of gadolinium are selected. These samples are listed as follows:

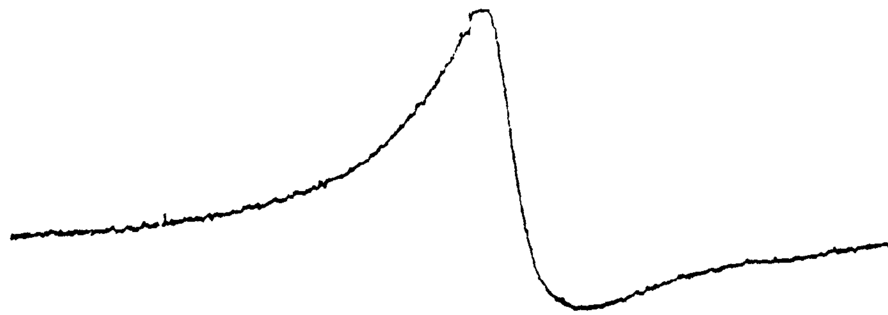

(a)

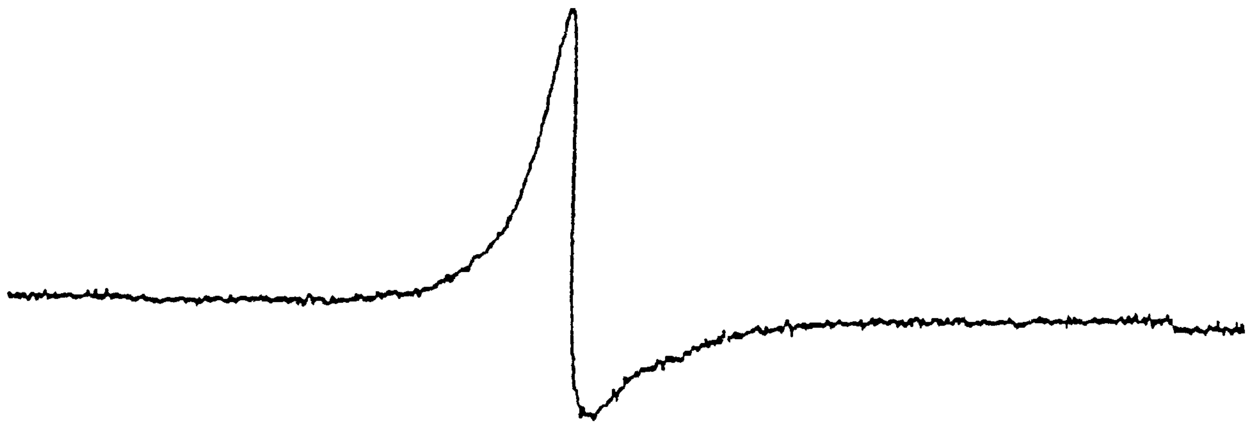

(b)

Figure 3.4 EPR spectra of a PbGdTe sample with $x = 1\%$.

(a) – Field range : + 250 gauss.
(b) – " : + 1000 gauss

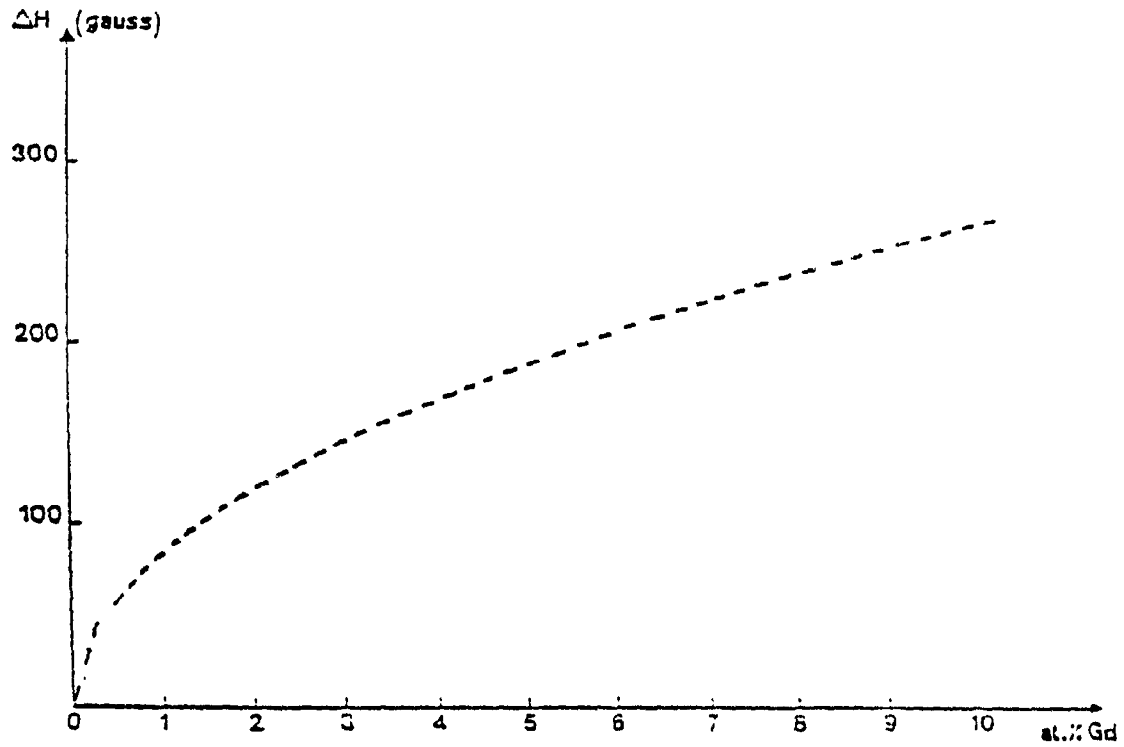

Figure 3.5 The variation of ΔH as function of the atomic percentage of gadolinium in the ternary compound PbGdTe.

Sample name	atomic % of Gd
M2	≃ 2
M6	≤ 0.25
M7	0
M10	≃ 5
M11	1

3.2.2 Electrical characterization of the samples

The expressions for the resistivity (equation 2.4), carrier density (equation 2.8) and electron mobility (equation 2.9) are determined for a 6-contact sample. The dependency of the resistivity of the samples on the temperature is shown in figures 3.6. The monotonic decrease of the resistivity is more pronounced for samples M6, M7 and M11 than for samples M2 and M10. Figure 3.7 shows the variation of carrier density n of sample M7, M6 and M11 versus the temperature. The variations of mobility of different samples versus the temperatures are shown in figure 3.8. For samples M7, M9 and M11, two distinct regions could be distinguished from the curves. In the temperature range from 300° K to around 30° K, the curve $\log(\mu)$ versus $\log(T)$ gives a straight line with a slope of $-3/2$. In the temperature range from around $30^{\circ}K$ to $4.2^{\circ}K$, the variation of the mobilities as a function of the temperature no longer obeys the $-3/2$ power law. The mobility increases continuously

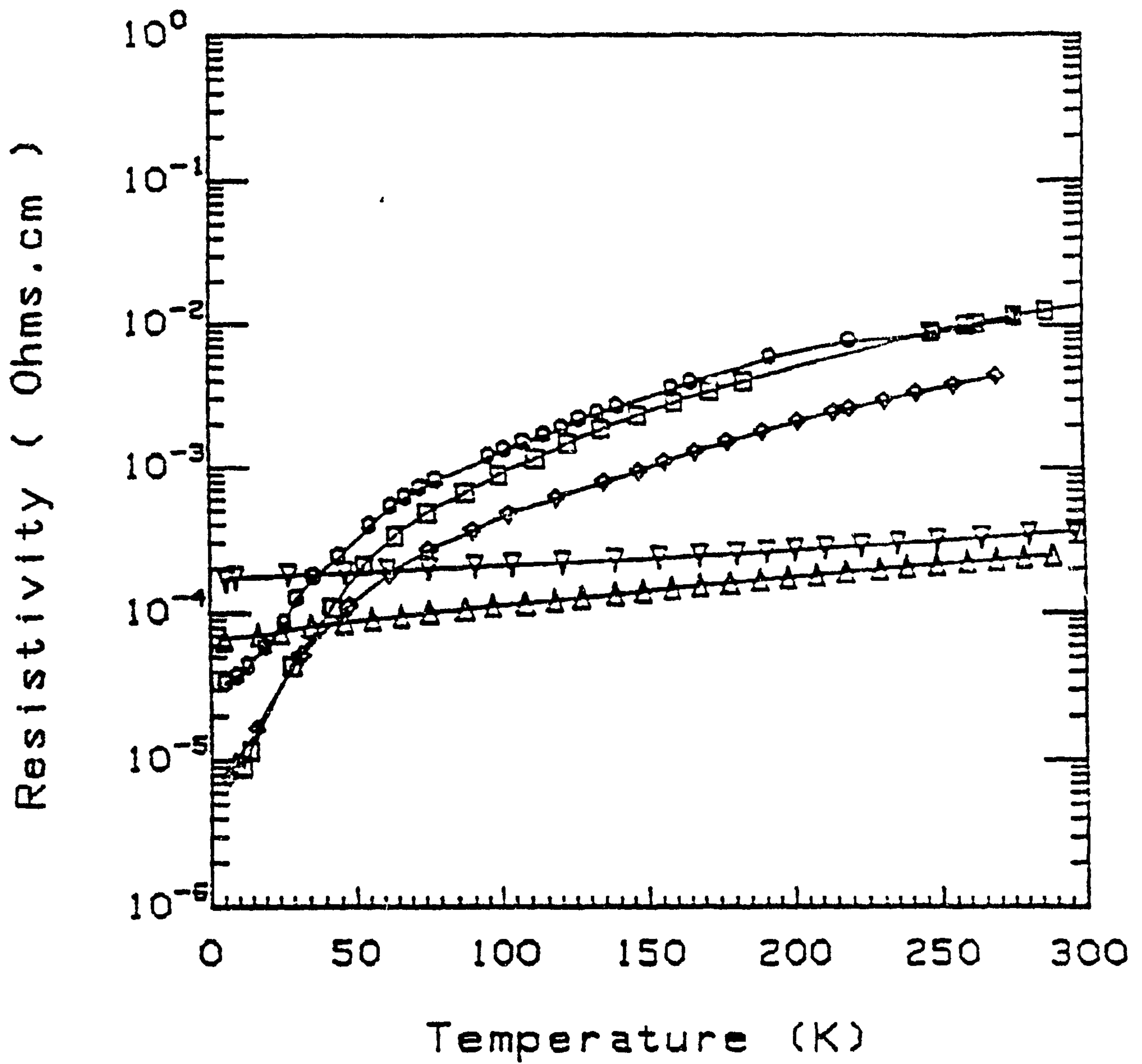

Figure 3.6 Resistivity of different samples as function of the temperature.
▽– M2 (x=2%)
◇– M6 (x less than 0.25%)
○– M7 (x=0%)
△– M10 (x~5%)
□– M11 (x=1%)

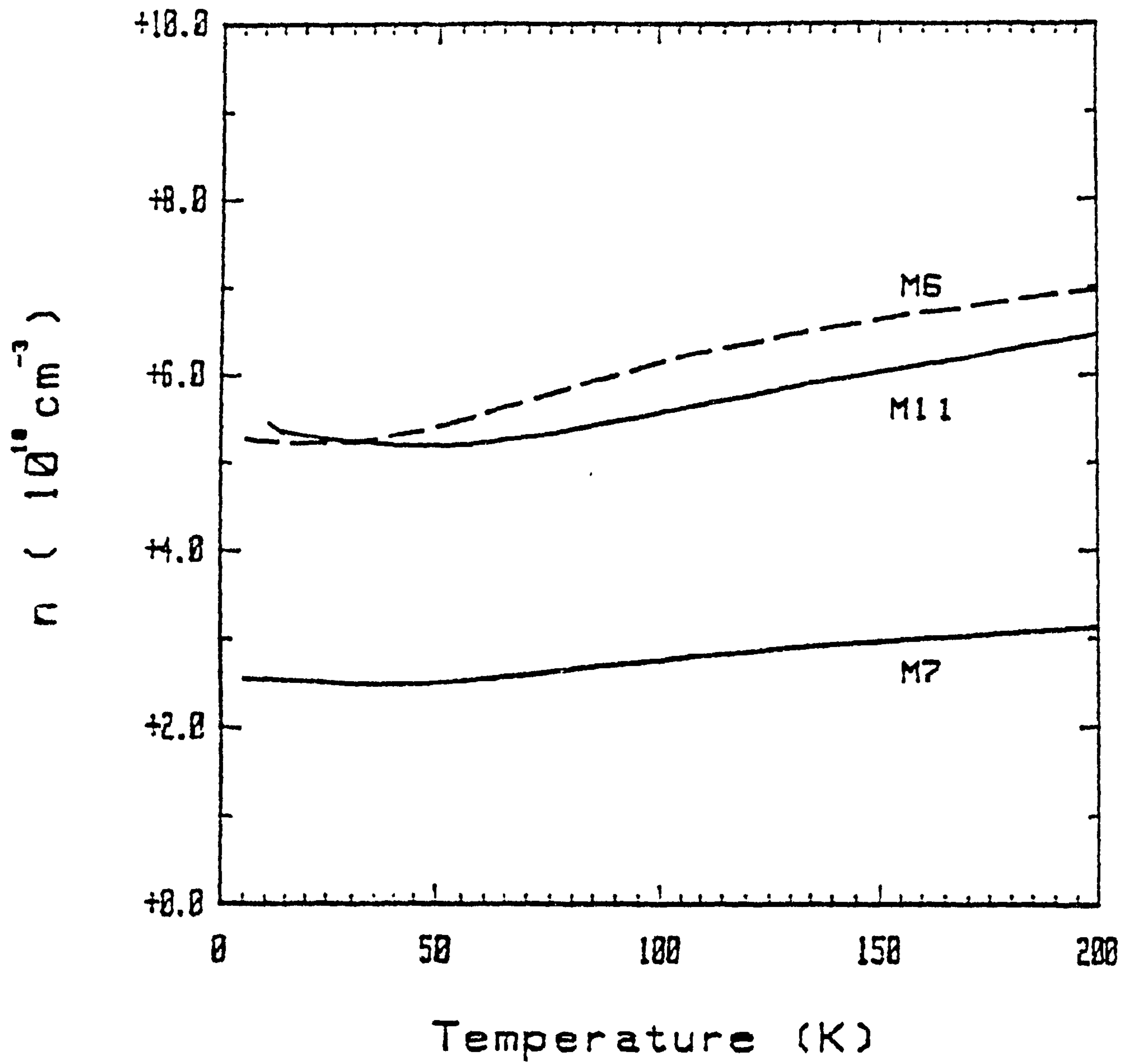

Figure 3.7 Carrier density of samples M6, M7 and M11 as function of the temperature.

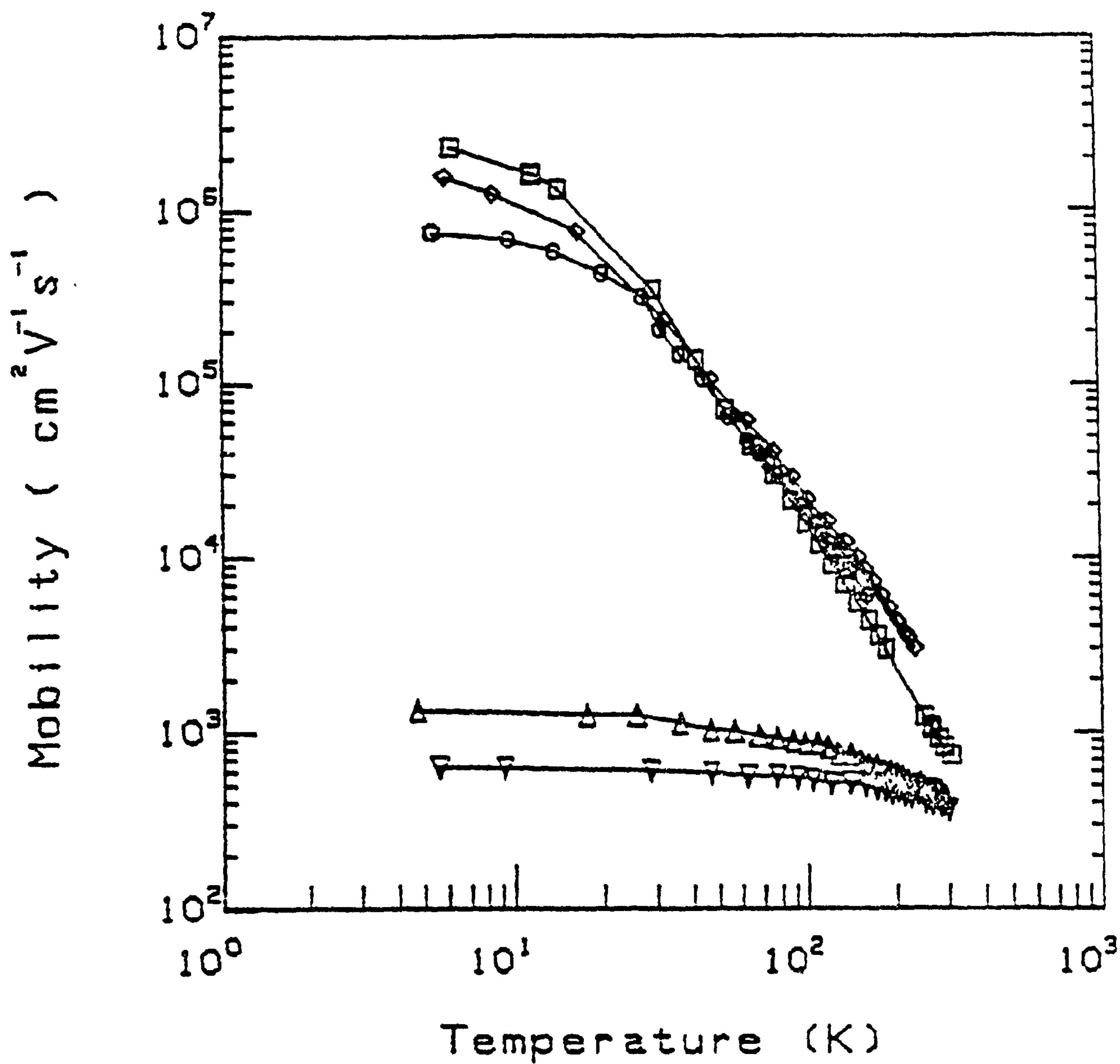

Figure 3.8 Carrier mobility of different samples as function of the temperature.
- M2 (x=2%)
- M6 (x less than 0.25%)
- M7 (x=0%)
- M10 (x~5%)
- M11 (x=1%)

until a maximum at 4.2°K. of mobility between the samples seems to be constant. The highest mobility ever obtained is in the range of 10^7 = 10^6 cm^2 V^{-1} s^{-1} as reported in [20,21,42] with a measured gadolinium concentration of 1%. These values are superior to the one reported in the case of the classical 2D superlattice of GaAs/GaAlAs modulated band structures.

3.3 Discussion

The concept of Wigner's crystallization is used to elucidate these very high electron mobilities of the "tachikinetic" electrons [21]. He has introduced the hypothesis of a formation of electron crystal in a homogeneous positively charged background [18]. After Wigner's model electrons in the presence of uniform space charge region created by a regularly arranged lattice of positive ions are submitted mainly to repulsive actions of surrounding charges. For very low temperature, their kinetic energies are less important than the energy from the Coulomb interactions. The electrons have then the tendencies to assume definite positions such that their potential energy will be a minimum. This results in the formation of a cubic lattice of the positive charges in order to decrease the energy of the ground state. A condition for this to occur is that the average distance between electrons is large, hence the density of the electron gas is low.

E. M. Chudnovski [36] has given a mathematical model for an electron lattice in an inhomogeneous medium (which is likely the one of most semiconductors). According to the results of the calculations, such charge lattice is most likely be destroyed by fluctuations in electric potential due to static fluctuations of impurity concentration. These fluctuations are of statistical nature and are formalized by B. Landau and E.M. Lifshitz [37]. In a randomly distributed donors system with a

total concentration N_a, a necessary condition for the formation of charge lattice is $N_e = N_a^- - N_a^+ << N_d^o$, where N_e, N_d^o, N_d^+, N_a^+ are respectively the concentration of free-electrons, the concentration of neutral donors, the concentration of ionized donors and the concentration of ionized acceptors. Hence in compensated semiconductors, the condition of low electron density may not be realized if the density of neutral positive impurities which do not participated to the mechanism of compensation is not large enough to allow the redistribution of the charges.

In the case of $Hg_{1-x}Fe_xSe$, A. Mychielski *et al* [38] have shown that the transition metal Fe^{2+} acts like a neutral resonant donors with an energy level being many KT above the conduction band. After J. Mychielski [15], the presence of this narrow state will spin the Fermi level and thereby the free electron concentration will become independent of further increase of the total donor concentration. Measurements of electron concentrations of various $Hg_{1-x}Fe_xSe$ samples show that, while N_d is in order of 10^{20} cm^{-3}, N_e varies around a mean value of $5x10^{18}$ cm^{-3}. Since the requirement $N_e << N_d$ is respected, the hypothesis of space-ordering of ionized donors and the formation of 3D superlattice can be invoked to explain the abnormal high measured electron mobilities. As for $Pb_{1-x}Gd_xTe$, the substitutional magnetic ion Gd^{3+} may hold the same role as Fe^{2+} in $Hg_{1-x}Fe_xSe$ by introducing a resonant donor level situated at few KT above the conduction band. The

4f electrons of Gd participate to the conduction process even if 4f states are very localized and the orbital overlaps are negligible (~ [illegible] angstroms). The atomic percent x of gadolinium measured by EPR give an equivalent concentration of donors impurity in the order of 10^{20} cm^{-3} [illegible] $< x \leq 0.05$).

While transport measurements give a steady free electron concentration for the temperatures ranging from 20°K to [illegible]°K about [illegible] cm^{-3}. Which is less than the effective donors concentration. Thus, once again the basic requirement of Wigner's crystallization, $N_e \ll N_d$ is satisfied. The expression for the mobility can be obtained from the standard formula for elastic scattering in a degenerate semiconductor with a simple spherical conduction band:

$$\mu = \frac{e\,\tau}{m^*} \qquad (V^2.cm^{-1}s^{-1}) \qquad (3.5)$$

where τ is the total momentum relaxation time for the free electron system and m^* is the effective mass of the electron. An expression of τ is given by Pool *et al* [16] which take into account the standard deviation of ionized donors lattice site positions from perfect periodicity. However, by assuming a Bravais type superlattice with strong deflection and deformation, an approximate expression for the lattice mobility is given by J. Mychielski [15]:

$$\mu_{latt} = \left[\left(\frac{18\,\pi\,h^3\,K^2}{e^3\,m^{*2}\,s}\right)\left(1 + \frac{q_{TF}}{2\,k_F}\right)^2\right]^2 \qquad (3.6)$$

Where q_{TF} is the Thomas-Fermi screening radius, K is the static dielectric constant of the crystal, h is the Planck's constant, k_F is the Fermi wavevector and s is the number of nearest neighbours in the reciprocal lattice (s is equal to 8 for f.c.c., 6 for s.c. and 12 for b.c.c.). For a system with a low density degenerated electron gas, q_{TF} is given by:

$$q_{TF} = \frac{\hbar}{2\ e} \frac{K_*}{m} \left(\frac{\Pi}{3\ N_e} \right)^{1/3} \quad (3.7)$$

For $Pb_{1-x}Gd_xTe$, the parameters of the last equation are $m = 0.034\ m_o$ where m_o is the rest mass of the electron, K = 400, $N_e = 6x10^{17}\ cm^{-3}$ and $N_d = 2x10^{20}\ cm^{-3}$. Which gives a mobility of $\mu = 5.7x10^7\ cm^2.V^{-1}.s^{-1}$. The highest measured mobility reached so far is for sample M11 with x = 1%. Mobilities in the order of $1.1x10^7\ cm^2.V^{-1}.s^{-1}$ have been reached [20] and this value is higher than the one allowed by calculations which take into account different scattering mechanisms [39, 40]. In figure 3.9, top measured mobilities for $Pb_{1-x}Gd_xTe$ at 4.2 K as a function of electron concentration for n-type sample are plotted with calculated electron mobilities for PbTe due to acoustical phonon combined with coulombic scattering, the one due to acoustical phonon only and experimental data published by Granger *et al* [40]. In such case, Wigner electron crystal may be a likely hypothesis to explain the abnormal measured results [20, 41, 42].

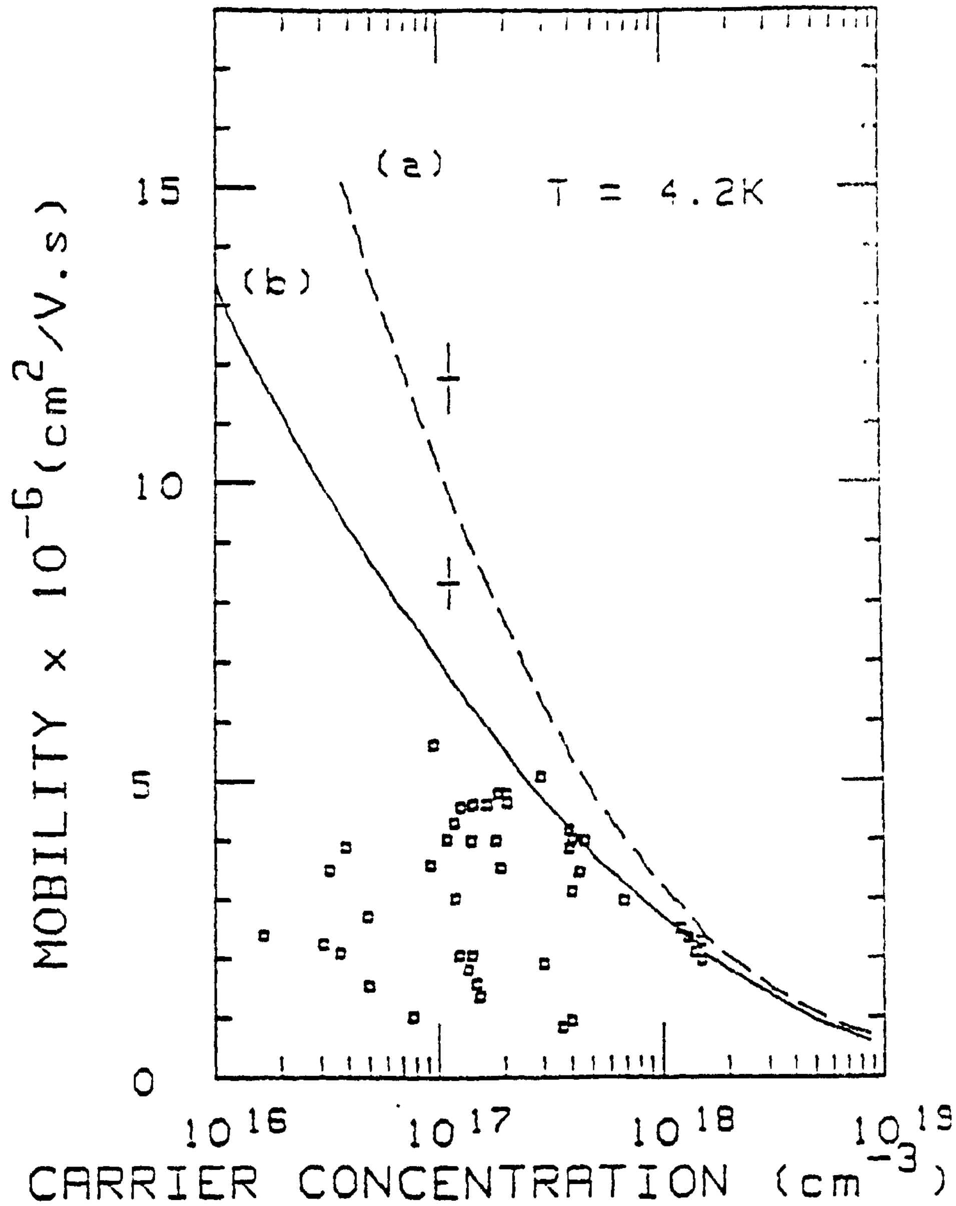

Figure 3.9 Comparison between calculated and measured mobilities at 4.2K of PbTe and top mobilities measured in PbGdTe as the function of electron concentration for the n-type sample.

(a) - Calculated mobilities considering accoustical phonons.
(b) - Calculated mobilities considering phonon and charged center scattering.
□ - Experimental data for PbTe published by Granger et al [40].
+ - Experimental data for PbGdTe.

CHAPTER 4

PREPARATION AND CHARACTERIZATION OF EPITAXIAL LAYERS OF GaAs

The Close-Space Vapor Transport technique is an alternative crystal growth technique to CVD (Chemical Vapor Deposition). The primary idea behind this technique is to bring together the source and the substrate in a manner that the distance which separates them is less the mean free path of reactive elements [43,44,45]. Then, the gas-phase mass transfer is induced by the displacement of the thermodynamical equilibrium constant, induced by the different source and substrate temperatures, of the transport reaction. Using this technique, low pressure environment is not required as in the case of MBE (Molecular Beam Epitaxy). Furthermore, the use of water vapor eliminate the need for toxic agent such as arsine used in MOCVD (Metal-organic Chemical Vapor Deposition). This growth process will be briefly described in the following sections. Defects associated to GaAs layers grown with this technique will be characterized by Deep-Level Transient Spectroscopy while their transport properties will be evaluated by measurements such as Hall effect.

4.1 Samples preparation

4.1.1 Epitaxial growth by Close-Space Vapor Transport technique (CSVT)

The schematic diagram of the CSVT setup is shown in figure 4.1. The reaction chamber is made of fused silica and contains two graphite blocks as heat susceptors. The surfaces of the source and the substrate are separated by fused silica spacer with a thickness in the range of 0.5 to 0.3 mm. The heat source is a set of 2-kW glowbar (SiC) heating elements The temperature regulation is done using two thermocouples positioned in appropriate wells inside the graphite blocks, a temperature controller Barber-Colman and a cold air flux. The transport agent is wet hydrogen containing distilled water vapor corresponding to a saturator temperature of 0^0C (the partial vapor pressure is then around 4.58 torr).

CSVT is based on the reversible chemical reaction between GaAs and H_2O, which performs also the role of transport agent. The main transport equation is :

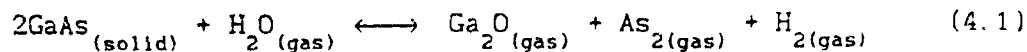

$$2GaAs_{(solid)} + H_2O_{(gas)} \longleftrightarrow Ga_2O_{(gas)} + As_{2(gas)} + H_{2(gas)} \qquad (4.1)$$

and

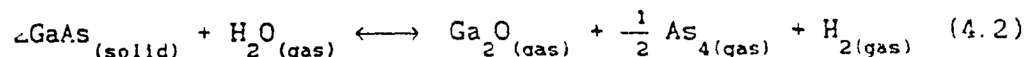

$$2GaAs_{(solid)} + H_2O_{(gas)} \longleftrightarrow Ga_2O_{(gas)} + \frac{1}{2} As_{4(gas)} + H_{2(gas)} \qquad (4.2)$$

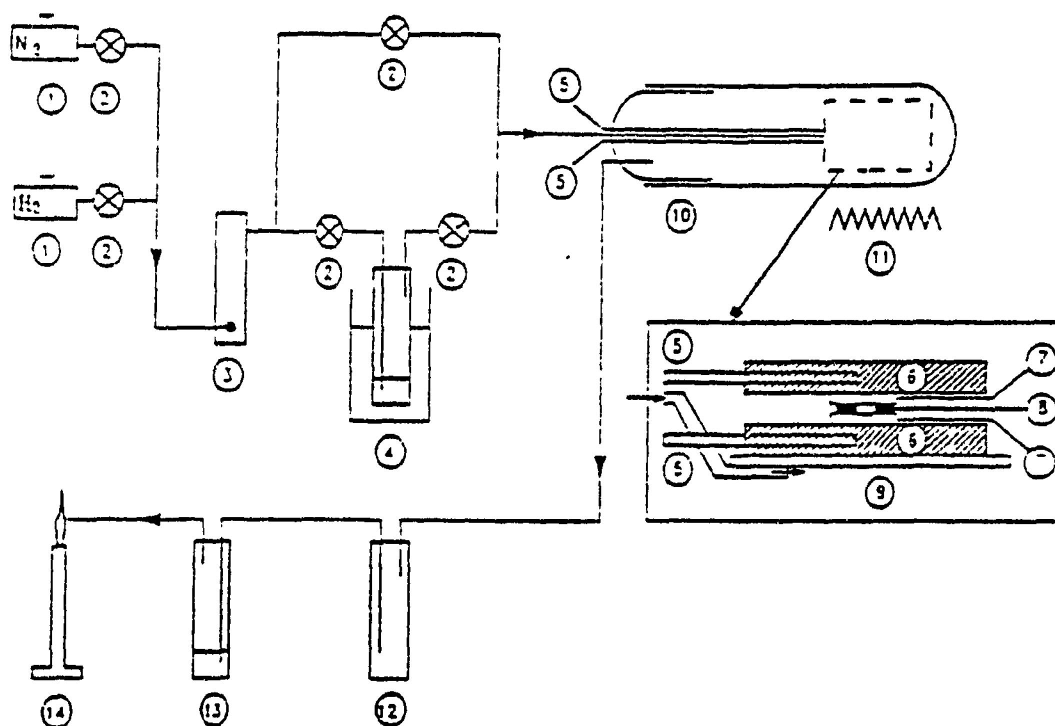

Figure 4.1 Schematic representation of the CSVT deposition system.

1. N_2 and H_2 gas cylinders
2. Valves
3. Flow meters
4. Water saturator
5. Thermocouples
6. Graphite blocks
7. Spacer
8. GaAs source and substrate
9. Gas exhaust
10. Fused silica reactor tube
11. 2000 W glowbar (SiC) heater
12. Trap
13. Glycol bubnler
15. Burner

These reactions are in thermodynamic equilibrium at the surface of the source and the substrate. When a gradient of temperature is imposed such as $T_{source} > T_{substrate}$, the position of equilibrium is displaced the reactions (4.1) and (4.2) are shifted from the left to the right at the surface of the source and vice-versa at the surface of the substrate. The transport of GaAs is done by the diffusion of gaseous species, ie. Ga_2O, As_2 and As_4.

At the beginning of the cycle of the crystal growth process, the source and substrate are degreased in hot trichloroethane, acetone, methanol and then rinsed in deionized water. The etching is done with a solution of $H_2O:NH_4OH:H_2O_2$ (150:6:1) for about 2 minutes and then rinsed in deionized water. The source and the substrate are then sandwiched between the two heat susceptors in the reaction chamber. The growth cycle starts by the flushing of the chamber with a flux of nitrogen and then with a flux of dry hydrogen prior to the introduction of wet hydrogen. At this point, the temperature is quickly raised while the temperature gradient ΔT is maintained as close as possible to the desired value (within the range from 40^0C to 30^0 C). The temperature range of the epitaxial deposition was $750-880^0C$. The growth rate is relatively high and can be up to 60 $\mu m/hr$.

The substrates were (100) oriented semi-insulating (SI) non-intentionally doped GaAs. Three types of sources are used for the

preparation of the samples: SI undoped, Si-doped and Zn-doped (100) oriented GaAs wafers. Good mirror-like effects were observed for all selected samples. The average thickness of the deposited layers ranged from 4 μm to 10 μm.

4.1.2.1 Fabrication of Hall devices

The transport properties of the sample were determined from Hall-effect measurements using the Van-der-Pauw technique. Prior to the fabrication of the Schottky diode on the same sample, four ohmic contacts were formed (mostly on the boundaries of the epitaxial layer). the contacts were prepared on the samples using indium alloyed for 2 minutes in hydrogen atmosphere at 430°C. One of these contacts is later used as background ohmic contact for the Schottky device.

4.1. Fabrication of Schottky devices

The capacitive characterization techniques such as the DLTS using Schottky diodes is used for investigation of bulk traps in semiconductor material. It is shown that the DLTS signals for mid-gap electron traps in n-type GaAs depend on the value of the Schottky barrier height ϕ_B [46,47] and the behavior of the interface as well [48]. Therefore, in order to fully be able to measure the main trap EL2 in GaAs [5], the barrier height of the Schottky contact must be at least superior to 0.82

eV (at room temperature). Since the quasi-Fermi level depends on the Schottky barrier height, all of the EL2 states are empty in the depletion region for a barrier height greater than 0.82 eV

To satisfy this requirement, an Al-Pd metallization system is used to fabricate Schottky diodes on n-type GaAs epitaxial layers. The used procedure is summarized as follows: i) classical degreasing in trichloroethane, acetone, methanol and rinsing with deionized water; ii) definition of the contact pattern using photoresist; iii) surface cleaning and palladium activation; iv) aluminum evaporation, v) contact revelation (0.8 mm diameter) by acetone "lift-off" process. A detailed description of each process is given in appendix C. The indium ohmic contact previously prepared and the spacing between the Schottky was more than 2 cm.

4.2 Experimental results

The Hall-effects measurements, capacitance-voltage, current-voltage characteristics and the DLTS studies have been performed using the same setup as described in chapter 2. The samples are classified into category A, B and C upon the sources used which are respectively SI, Si doped and Zn doped. Eventually, measurements on sample from the bulk crystal are performed for comparison purposes.

4.2.1 Hall-effect measurements

Measured carrier mobilities at 77K versus the carrier concentration of the samples grown using SI sources is shown in figure 4.2. Also plotted in this figure are theoretical computations of electron mobilities based on variational method including all major scattering processes [49]. At room temperature, The carrier concentrations are in the range of $5x10^{15}$ to $2x10^{17}$ cm^{-3} for samples in category A, $2x10^{16}$ to $5x10^{17}$ cm^{-3} for samples in category B, and less than 10^{19} cm^{-3} (p-type) for samples in category C. The measured carrier mobilities measured at room temperature are 4200 $\pm$ 500 cm^2/V s for samples A, and less than 3000 cm^2/V s for other samples. The low carrier mobilities measured for samples of category B and C suggest the presence of heavily compensated materials.

4.2.2 I-V measurements

The typical I-V characteristic for different temperatures of an Al/Pd Schottky diode on n-type GaAs epitaxial layer grown by CSVT technique is shown in figure 4.3. The value of V_o can be computed from this curve. The variation of V_o in function of KT/e is shown in figure 4.4. The linear dependency of V_o with respect to KT/e is observed until lower temperature where a deviation from linearity occurs. A least-square fit of the log(I) versus V data give a slope from which the

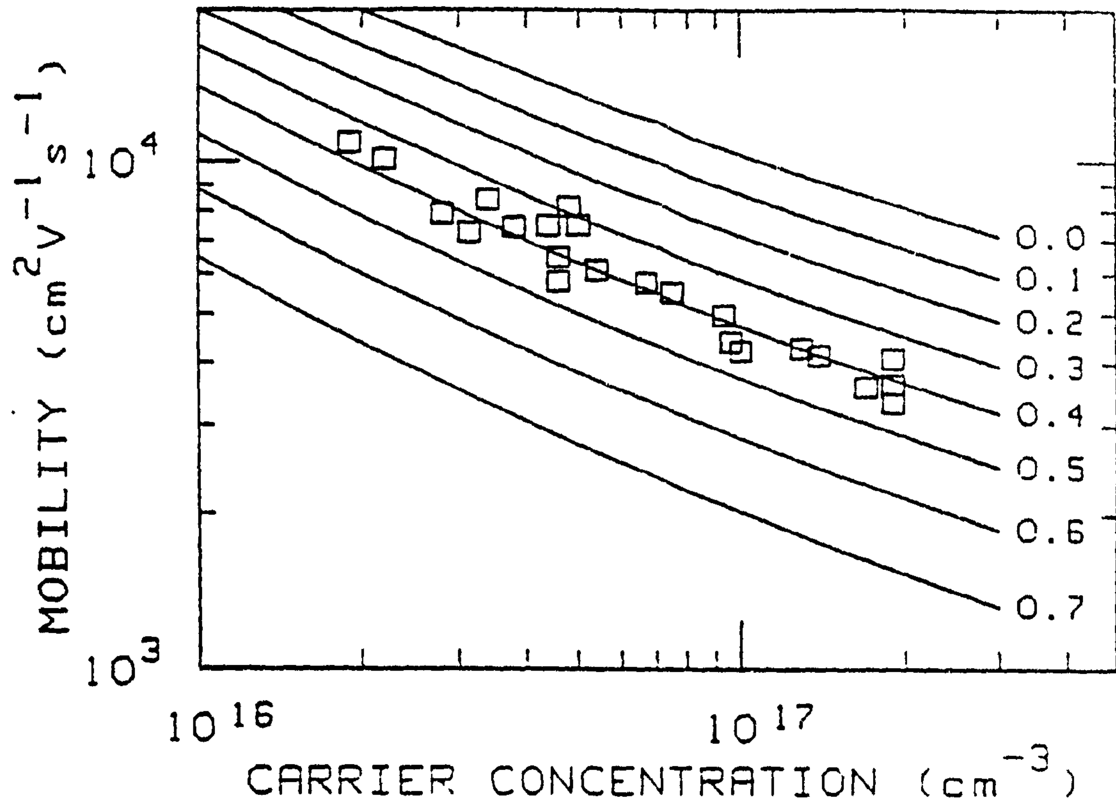

Figure 4.2 Comparison of electron mobilities in n – type GaAs grown from SI undoped source measured at 77K with W. Walukiewick [49] theoretical calculations for different compensation ratios.

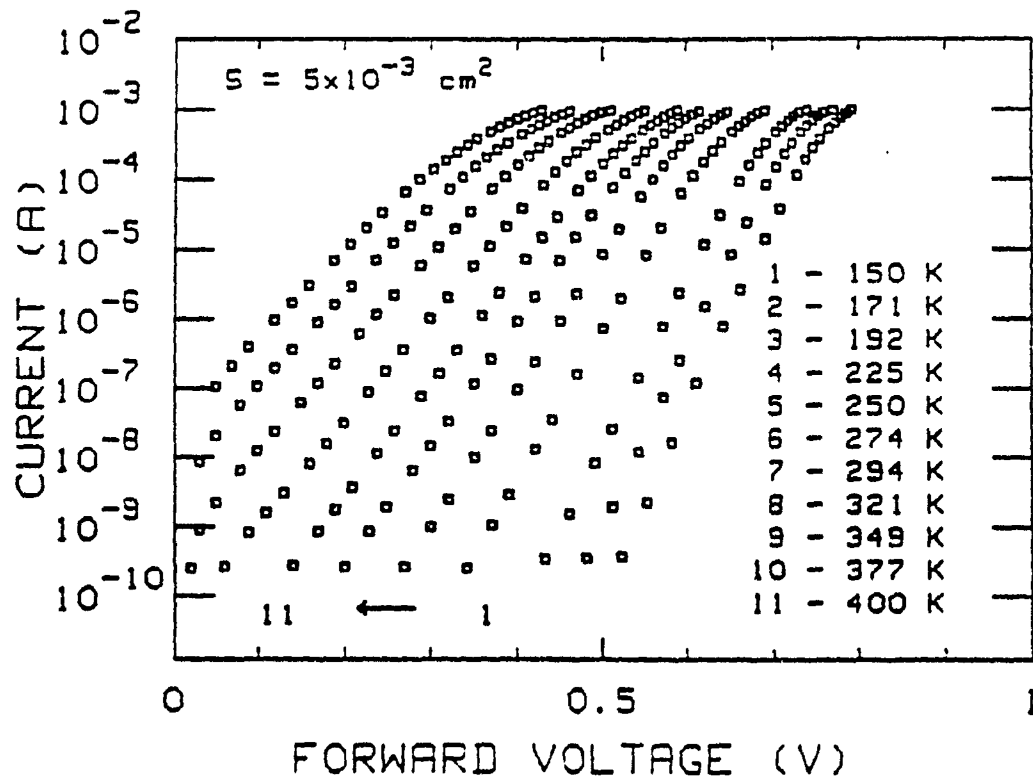

Figure 4.3 Forward semilog I–V plots given at different temperatures for an Al/Pd n–type GaAs Schottky diode. The temperature are labelled from right to left as 1 to 11 respectively.

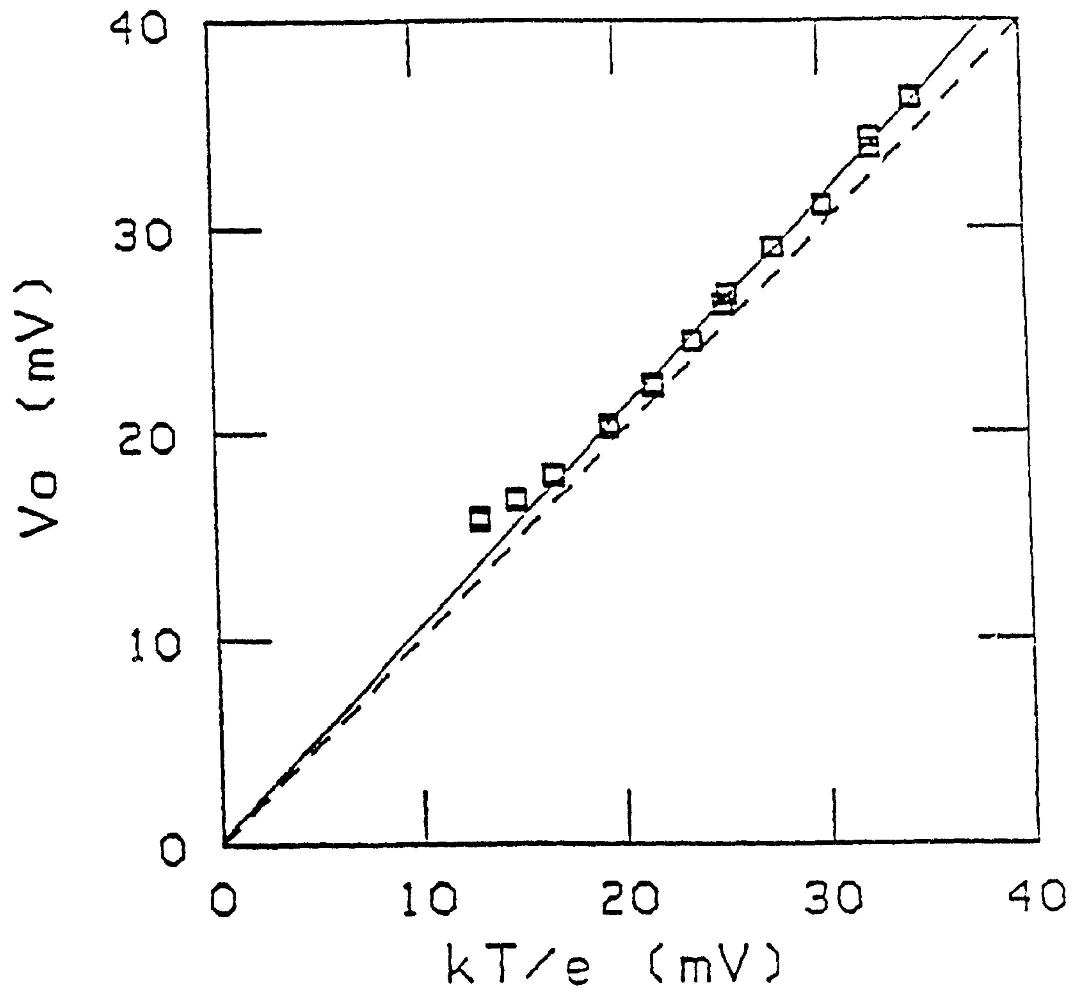

Figure 4.4 Plot of V_o versus kT/e. The solid line with a slope of 1.04 fits the experimental results while the dashed line represents the unity slope line.

ideality factor n is deduced. The temperature dependency of n is shown in figure 4.5. At temperatures above 200°K, n is constant and is about 1.04. For lower temperature, the behavior of n is similar to the one observed on some Schottky diodes made on silicon or GaAs [26,27,50] and can be expressed by the relation:

$$n = 1 + T_o/T \quad (4.3)$$

where T_o is a constant independent of the temperature named as "excess temperature". This may correspond to a particular distribution of interface states [51] and/or a non-uniformly doped surface layer [52] or some tunneling effects [53].

From the I-V curve obtained at room temperature, one can deduce the saturation current I_s which is equal to 4.84×10^{-12} A. Since the surface S of the metal-semiconductor contact is equal to 5×10^{-3} cm^2 and using a Richardson constant $A^* = 8.2$ A/cm^{2}K^2, the Schottky barrier height is calculated as being 0.86 eV. Thus, the EL2 data can be accepted.

4.2.3 C-V measurements

The curve $1/C^2$ versus the applied bias voltage at different temperatures is shown in figure 4.6. The doping concentration is deduced from the slope of this curve and is equal to 1.41×10^{16} cm^{-3}. This value

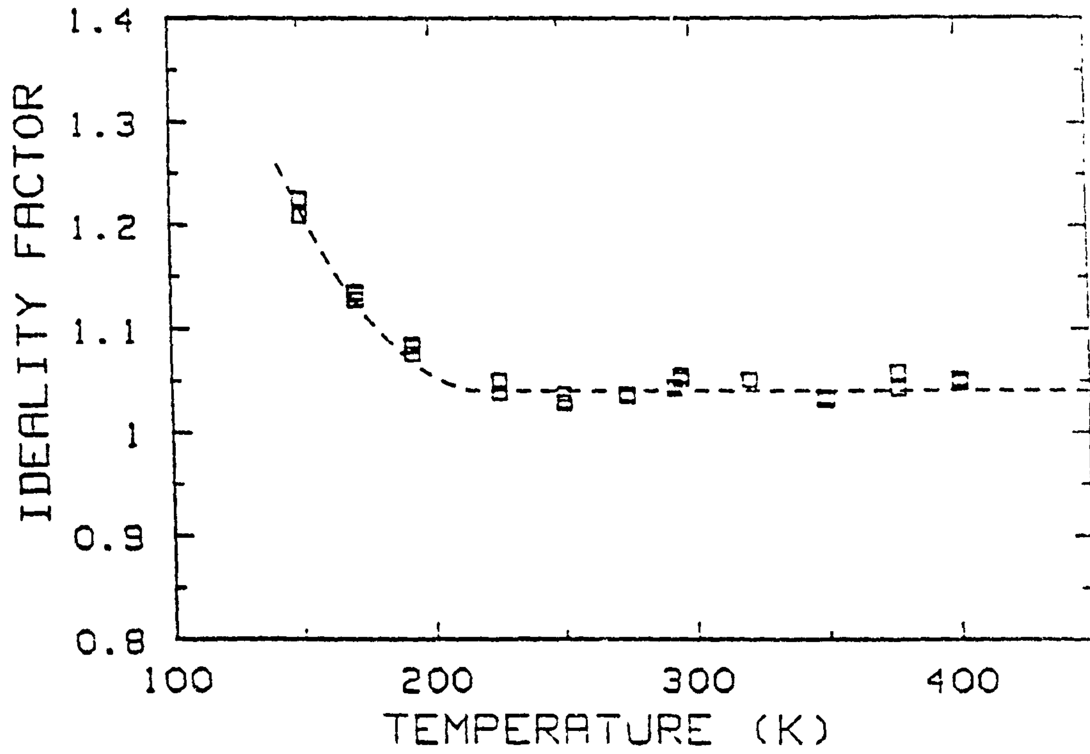

Figure 4.5 Variation of the ideality factor with temperature.

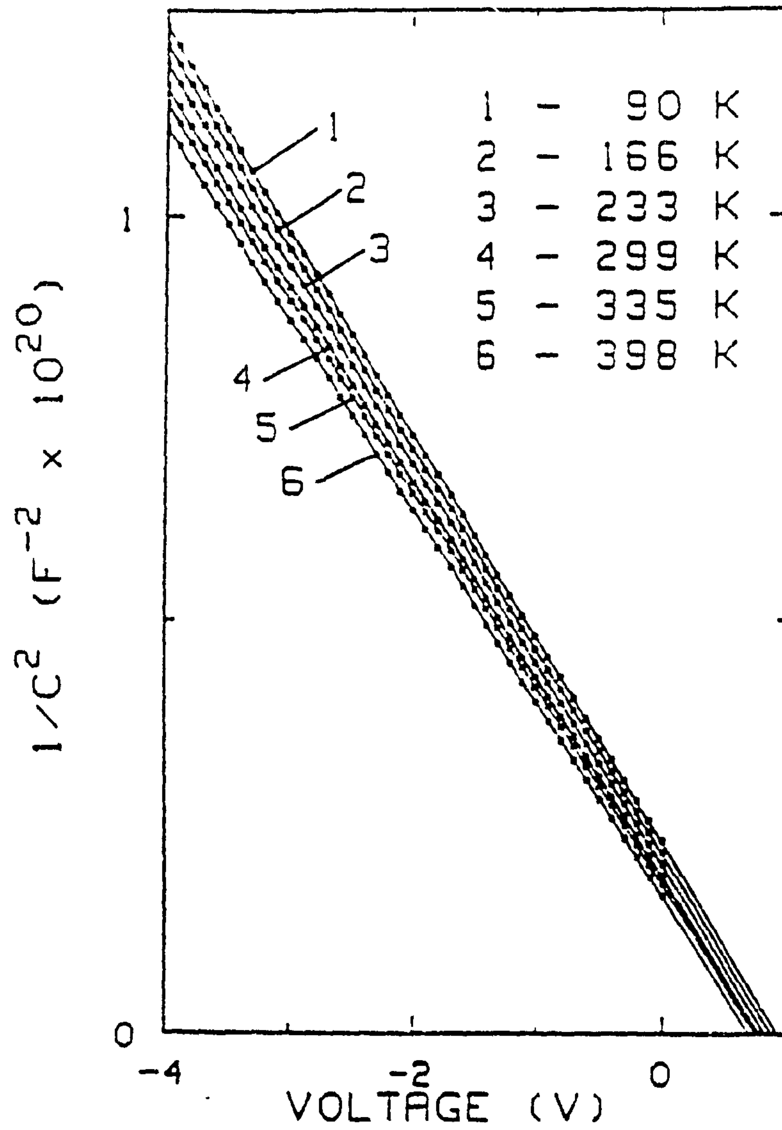

Figure 4.6 $1/C^2$ plot as a function of applied voltage for different temperatures.

is in agreement with the one obtained by Hall effect measurements. The intercept with the voltage axis gives the built-in potential V_{bi} as being 0.8 V.

4.2.4 Electron traps characterization by Deep Level Transient Spectroscopy

Typical DLTS spectra of two Al/Pd n-type GaAs Schottky diodes are shown in figure 4.7. The curve (A) and the curve (B) of this figure were obtained with a diode prepared on bulk material (Bridgman sample) and a diode prepared on CSVT epitaxial layer (deposited at a substrate temperature of 800° C). The emission rate was of 0.39 s (t_1 = 0.1 s, t_2 = 1.0 s). It can be seen from figure 4.7 that over the analyzed temperature range of 260°K to 360°K, one electron trap is detected in the sample from Bridgman. This electron trap is identified as deep donor level EL2, with an apparent activation energy ΔE of 0.81 eV and an apparent capture cross-section σ of 2.1×10^{-13} cm^{-2}. The concentration N_t of the EL2 deep donor trap was found to be 1.2×10^{16} cm^{-3}. In the case of sample obtained by CSVT, the presence of two electron traps can be observed from the DLTS spectra. Indeed, they were observed in most of the layers deposited by CSVT. These levels were labelled respectively ELCS1 and EL2. The apparent activation energy ΔE and the apparent capture cross-section for ELCS1 are respectively 0.71 eV and 1×10^{-13} cm^2. The deduced concentration of EL2 and ELCS1 for this particular layer are respectively 4.1×10^{13} cm^{-3} and 1×10^{15} cm^{-3}.

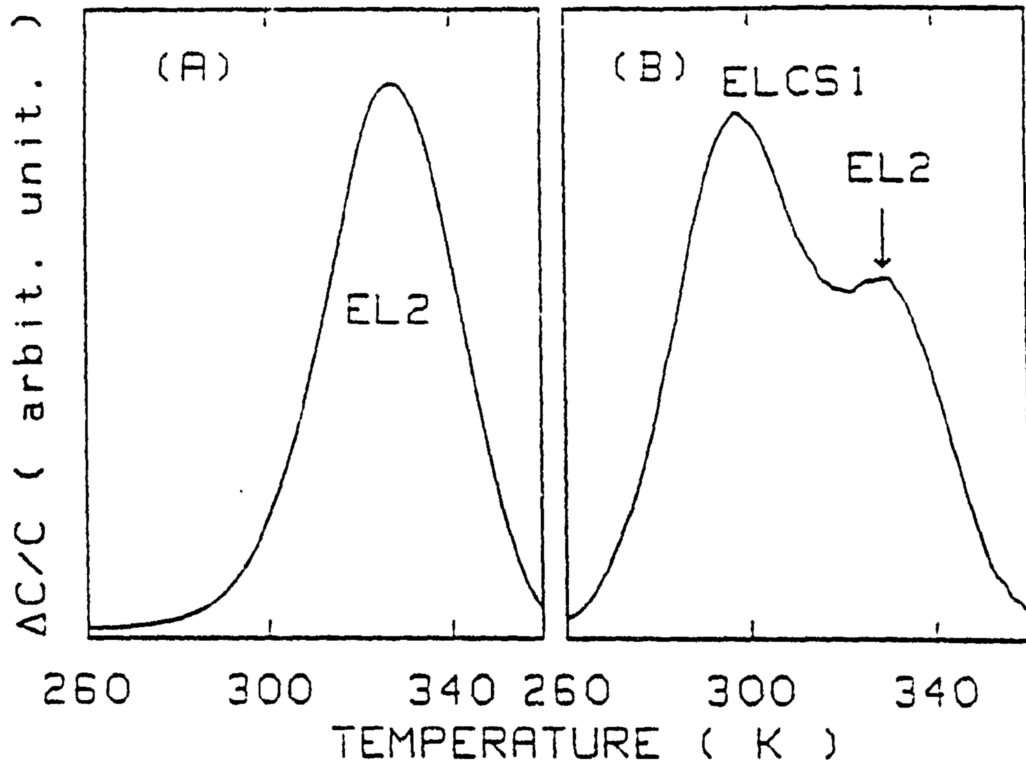

Figure 4.7 DLTS spectra of GaAs grown by Bridgman technique (A) and GaAs epitaxial layer (B) deposited by CSVT at a temperature of 850°C.

Figure 4.8 shows a DLTS spectra of two epitaxial layers grown at substrate of 850°C and 750°C for sample A1 (category A) and A2 (category A) respectively. The two electron traps EL2 and ELCS1 are visible and their concentrations are calculated using the equation (2.22). For EL2, the concentration of this traps in sample A1 and A2 are respectively $8.9\times10^{14}cm^{-3}$ and $9.3\times10^{12}cm^{-3}$. As for ELCS1, its concentration in sample A1 and A2 are respectively $3.8\times10^{12}cm^{-3}$ and $1.2\times10^{14}cm^{-3}$.

The DLTS spectra obtained for layers A2, B, and C, belonging respectively to the three categories A, B, and C, are shown in figure 4.9. For these measurements, the following settings are selected: the emission rate e_n is equal $2.56s^{-1}$ (t_2/t_1 = 10), the reverse bias is equal -1V and the filling pulse height is 1V. The carrier concentration for sample A2, B, C are respectively $7.3\times10^{15}cm^{-3}$, $5.6\times10^{16}cm^{-3}$ and $2.8\times10^{16}cm^{-3}$.

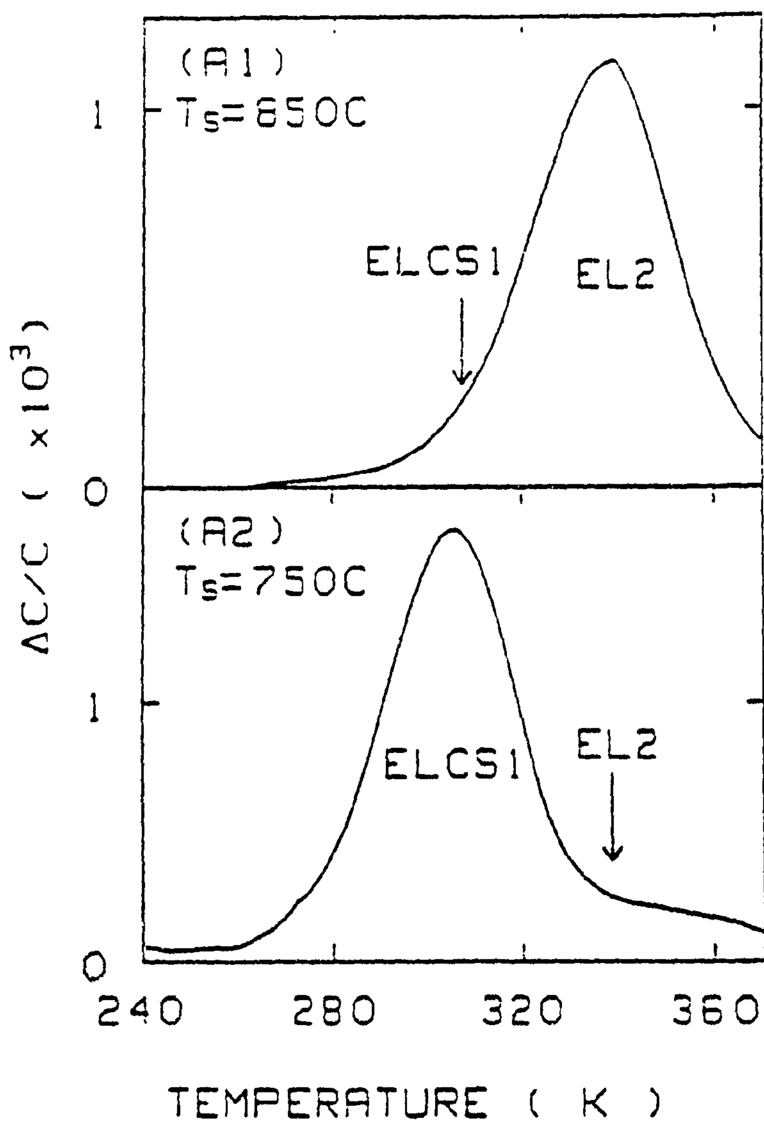

Figure 4.8 DLTS spectra of epitaxial layers grown at different substrate temperatures (a Si source was used).

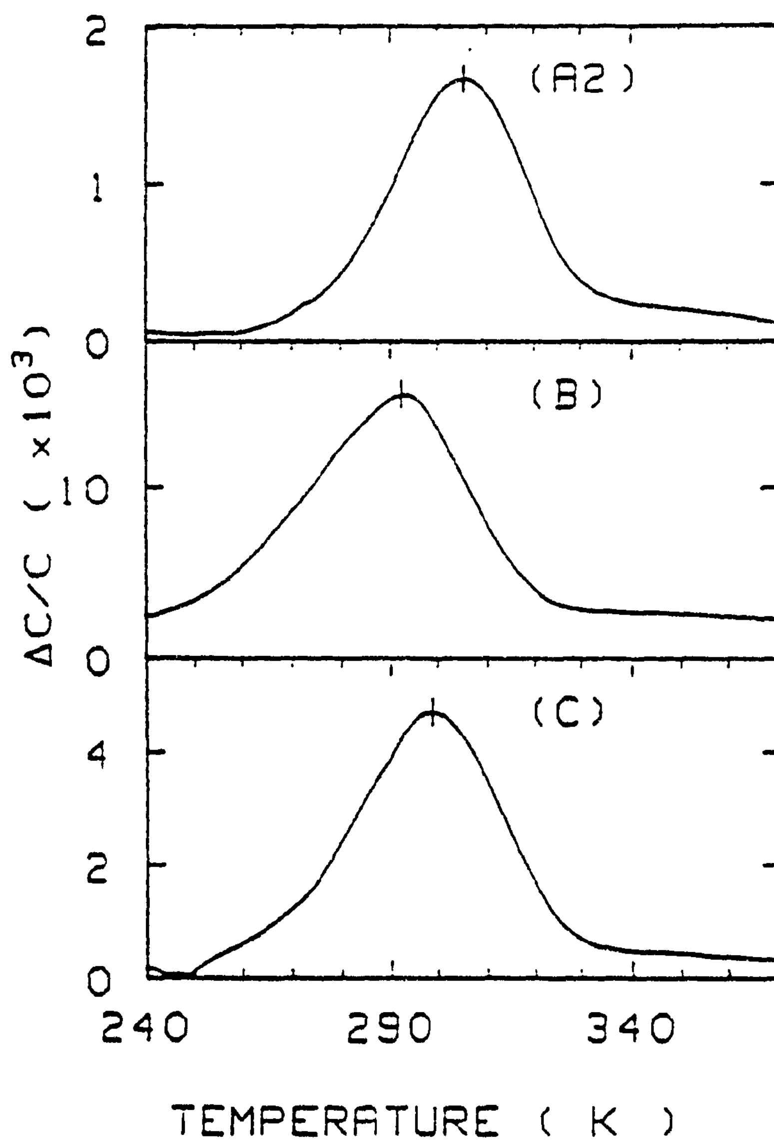

Figure 4.9 DLTS spectra of epitaxial layers grown with different kinds of sources: SI undoped (A2), Si-doped (B) and Zn-doped (C).

4.3 Discussion

The two electron traps, EL2 and ELCS1 were systematically observed in a dozen CSVT epitaxial layers deposited at various substrate temperatures. Detailed analysis on EL2 is given in [6]. The monotonic increase of the EL2 concentration as a function of substrate temperature between 750 and 860°C is shown in figure 4.10. EL2 concentration depends on the deposition temperature of the layers. Such a measured concentration range is comparable with the one of other epitaxial techniques such as vapor phase epitaxy (VPE) or MOCVD. The evolution of EL2 as a function of the possible off-stochiometry variation can be elucidated by using the multilevel analyses [54]. This analysis is based on one hand on the nature of the formation of the complex EL2, which is associated to an As vacancy and a substitutional arsenic antisite As_{GA}. On the other hand, the neutrality condition in n-type crystals requires, according to Shockley [55], the existence of a compensating deep acceptor level which allows the formation of SI GaAs. This deep acceptor is likely to be represented by the Ga vacancy from the antisite complex formed by a Ga vacancy and a substitutional gallium antisite Ga_{AS}. Then, accordingly to the multilevel impurity model, the EL2 concentration increases when the deposition temperature increases toward As-rich domain which is in agreement of experimental data.

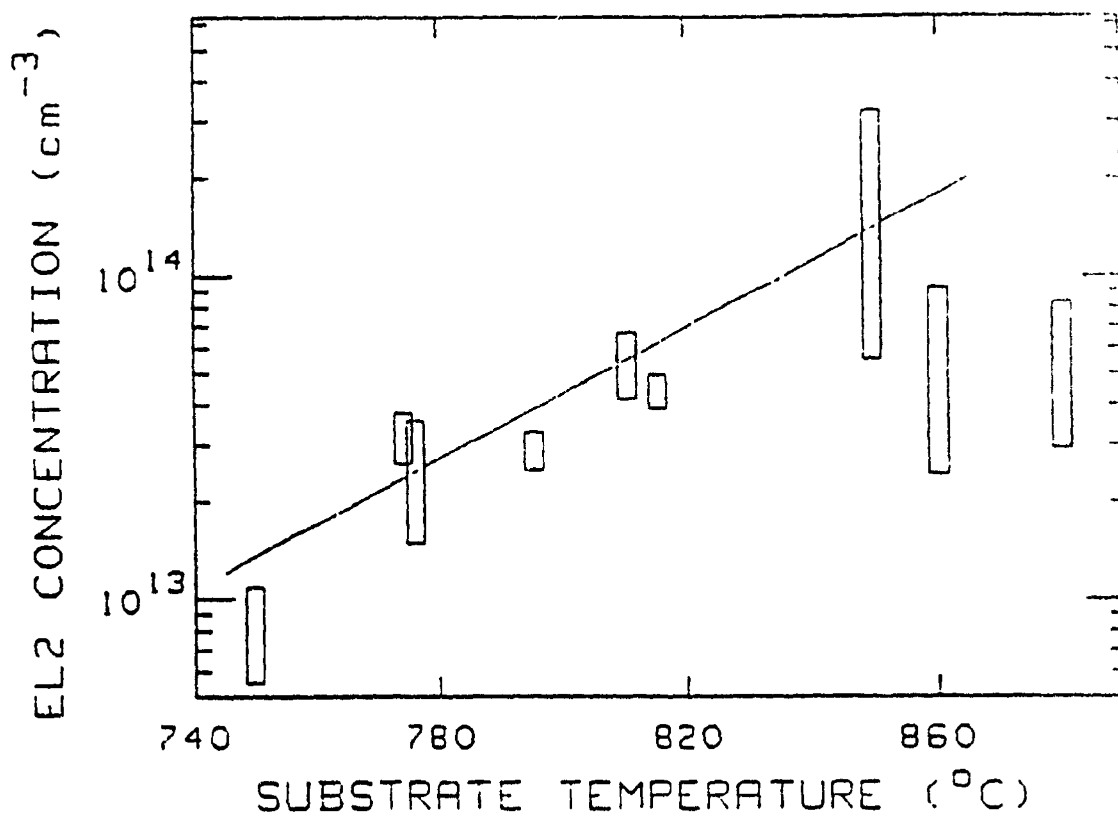

Figure 4.10 Evolution of EL2 versus substrate temperature.

The dependency of the concentration of ELCS1 on the carrier concentration of the layers is shown in figure 4.11. The layers belong to the three categories and are grown at 750°C. The concentration of ELCS1 in these layers follows the same trends and increases with increasing values of the free carrier concentration. In view of these results, it appears that the ELCS1 concentration is sensitive to the position of the Fermi level. Previous study [6] has shown that the ELCS1 level is present in relatively high concentration in the top few μm of the epitaxial layers grown using SI sources. It does not show any sign of existence in deeper region of the epitaxial layers.

The origin of the ELCS1 as well as its dependence on the concentration-growth conditions are not fully determined at the moment. However, a comparison of the thermal signature of ELCS1 to the one of electron traps reported for GaAs grown with other techniques can provide some guideline for further study. Similarities are found between the thermal signature of ELCS1 and the one of ETX2 (ΔE_T = 0.75 eV, σ = 1×10^{-12} cm^{-2}) and EL12 (ΔE_T = 0.78 eV, σ = 4.9×10^{-12} cm^{-2}). Figure 4.12 shows the Arrhenius plots of ELCS1 of two samples showing a doping level of $2.2\times10^{15}cm^{-3}$ (open square) and $3.2\times10^{16}cm^{-3}$ (closed square). On the same figure, are included the Arrhenius plots of ETX2 as given by Taniguchi [12] and EL12 as given by Micea [56]. The signature of deep level ETX2 is reported for a sample of GaAs grown by LEC (Liquid Encapsulated Czochralsky) with a free carrier concentration in the range of $2\times10^{15}cm^{-3}$ to $6\times10^{15}cm^{-3}$. The deep level EL12 is reported for

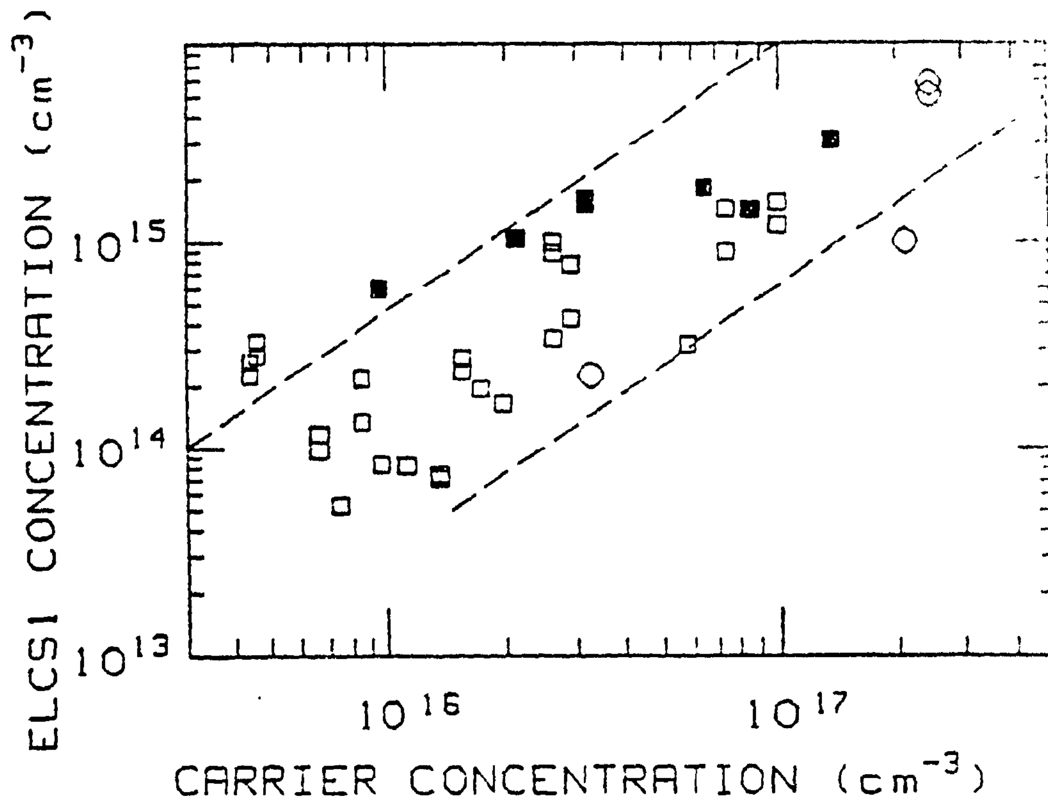

Figure 4.11 Variation of the concentration of ELCS1 versus the carrier concentration for samples grown using different sources:
□ – SI undoped.
○ – Si-doped.
■ – Zn-doped.

epitaxial layers deposited by VPE (Vapor Phase Epitaxy) with a doping level around $10^6 cm^{-3}$. From figure 4.12, an agreement can be noticed between the Arrhenius plot of ETX2 and our results corresponding to the lowest doping range (open square). Meanwhile, the Arrhenius plot of the sample with higher doping (closed square) is close to the one of EL12. Consequently, the experimentally observed ELCS1 trap could be identified either as EL12 or ETX2. According to the literature, these defects are related to complexes involving native defects associated to the kind of growth techniques such as LEC [12], VPE [52] and Bridgman [13] (the ETX2 trap is however not systematically detected in the case of melt growth techniques). This fact confirms that ELCS1 is a defect related to CSVT technique. Nevertheless, further studies are required to understand the exact origin of ELCS1.

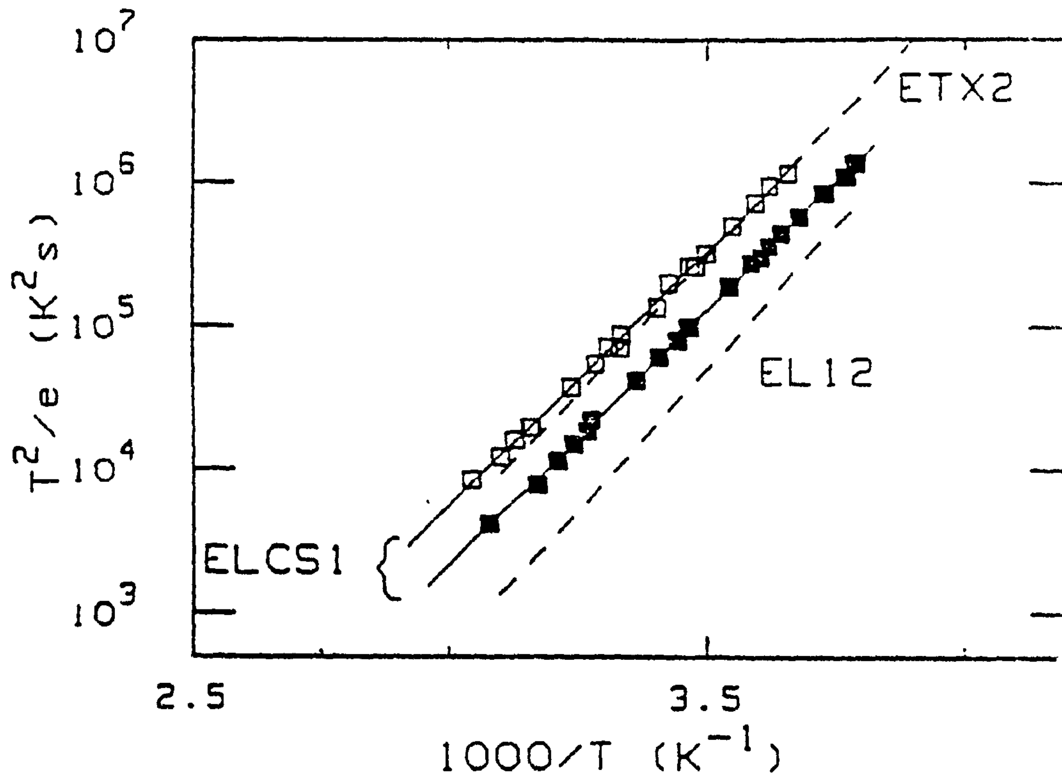

Figure 4.12 Arrhenius plot of ELCS1 of two samples with a doping level of $2.2x10^{15}$ cm^{-3} (□) and $3.2x10^{14}$ cm^{-3} (■). For comparison, published data on ETX2 and EL12 are represented by the dashed lines.

CHAPTER 5

CONCLUSION

Electrical properties of $Pb_{1-x}Gd_xTe$ and GaAs have been studied using computerized characterization systems. Included in the system is the setup for DLTS measurements which allow the study of main electron traps in n- type GaAs epitaxial layers. Those layers are grown by CSVT technique and using different kind of sources. Two deep donor EL2 and ELCS1 were detected in all of the above samples. The concentrations of ELCS1 measured in the layers grown using Si-doped and Zn-doped sources were found to be in the same range as the one in samples grown with an SI undoped source. A comparison of its Arrhenius plot with published data led to the identification of ELCS1 to ETX2 and EL12. Those traps are present in GaAs grown by either the LEC, VPE or Bridgman techniques and are attributed to a complex involving native defects.

Samples of $Pb_{1-x}Gd_xTe$ with $0 \leq x \leq 0.05$ have been synthesized and their transport properties have been measured using alternatively the Hall effect set-up at Concordia University and at USTL. The effective atomic percentage x of gadolinium is determined by EPR. The variation of mobilities in function of the temperature for samples with $0 \leq x \leq 1$ exhibits the -3/2 power law in the temperature range $20^{o}K \leq T \leq 300^{o}K$. This suggests that carrier scattering is due mainly to optical phonons in this temperature range. As in the case of $Hg_{1-x}Fe_xSe$, the electron

mobility for the temperature range $4.2^{\circ}K \leq T \leq 20^{\circ}K$ is very high and is function of the atomic percent x of gadolinium. Peak mobility (μ $cm^2.V^{-1}.s^{-1}$) is obtained for sample with x = 1%. This temperature dependence of the tachikinetic electron mobility can be interpreted the result of a spatial ordering of the charges within the donor as stated by Wigner's hypothesis.

REFERENCES

1. R. Castenedo, J. Mimila-Arroyo, and J. C. Bourgoin, J. Appl. Phys 68, 6274 (1990).

2. B. G. Russel and D. L. Pulfey, Proceeding of the 12th IEEE Photovoltaic Spec. Conf., 962 (1976).

3. J. Mimila-Arroyo, J. A. Rey, R. Legros and F. Chavez, Proceeding of the 16th IEEE Photovoltaic Spec. Conf., 952 (1982).

4. D. V. Lang, J. Appl. Phys. **45**, 3023 (1974).

5. Q. Y. Ma, M. T. Schmidt, X. Wu, H. L. Evans and E. S. Yang, J. Appl. Phys. 65, 2469 (1988).

6. B. A. Lombos, T. Bretagnon, A. Jean, R. Le Van Mao, S. Bourassa and J. P. Dodelet, J. Appl. Phys. 67, 1879 (1990).

7. D. Miller, G. H. Olsen, and M. Ettenberg, Appl. Phys. Lett. **31**, 538 (1977).

8. L. B. To, R. N. Thomas, G. W. Eldridge, and H. M. Hobgood, Inst. Phys. Conf. Ser. **65**, 31 (1983).

9. J. Lagowski, M. Kaminska, J. M. Parsey, H. C. Gatos, and W. Walukiewicz, Inst. Phys. Conf. Ser. **65**, 41 (1983).

10. S. Henghui, and . Chi, Inst. Phys. Conf. Ser. 65, 49 (1983).

11. B. Hughes, and C. Li, Inst. Phys. Conf. Ser. 65, 57 (1983).

12. M. Taniguchi, and T. Ikoma, Inst. Phys. Conf. Ser. 65, 65 (1983).

13. J. Lagowski, H. C. Gatos, J. M. Parsey, K. Wada, M. Kaminska, and W. Walukiewicz, Appl. Phys. Lett. **40**, 342 (1982).

14. G. Bauer, Mat. Res. Soc. Symp. Proc. **89**, 107 (1987).

15. J. Mychielski, Sol. Stat. Comm. **60**, 165 (1986).

16. F. Pool, J. Kossut, U Debska, R. Reifenberger, and J.K. Furdyna, Mat. Res. Soc. Symp. Proc. 89, 169 (1987).

17. E. Wigner, Phys. Rev. **46**, 1002 (1934).

18. E. Wigner, Trans. Fara. Soc. **34**, 678 (1938).

19. C. Grimes, and G. Adams, Phys. Rev. Lett. **42**, 795 (1977)

20. M. Averous, B. A. Lombos, A. Bruno, J. P. Lascaray, C. Fau, and F. Lauwrence, Mat. Res. Soc. Symp. Proc. **84**, 141 (1987)

21 B. A. Lombos, M. Averous, C. Fau, R. Le Van Mao, F. Silvestre, and Jean, E-MRS Spring Meeting, Symp. Magnetic Thin Films, Multilayers and Superlattices, Strasbourg (1990).

22. ASTM f76-84, 155 (1984).

23. Van Der Pauw, J. Phil. Res. Rep., 13 (1958).

24. S. M. Sze, *Physics of Semiconductor Devices* (John Wiley and New York, 1981).

25. F. A. Padovani, and G. G. Sumner, J. Appl. Phys. 36, 3744 (196

26. A. N. Saxena, Surface Scien. 13, 151 (1969).

27. R. H. Bube: *Photoconductivity of Solids* (John Wiley, New York, 1

28. A. G. Milnes: *Deep Impurities in Semiconductors* (John Wiley, New York, 1973)

29. J. C. Bourgoin, and M. Lannoo: *Point Defects in Semiconductors* (Springer Series in Solid-State Science, vol. 35, 1983).

30. J. F. Dumas, Doctorat Thesis, Universite des Sceiences et Techn du Languedoc (1988).

31. W. Giriat, and J. K. Furdyna: *Semiconductors and Semimetals*, 25 (Academic Press, London, 1988).

32. M. P. Gomez, D. A. Stevenson, and R. A. Huggins, J. Phys. Solids 32, 335 (1971).

33. Y. Sato, M. Fujimoto, and A. Kobayaski, Jpn. J. Appl Phys (1963).

34. J. C. Brice, *The Growth of Crystals from Liquids* (North- Publishing Company, Amsterdam, 1973).

35. R. Czock, and A. Framcik, *Instrumental Effects in Homodyne Electron Paramagnetic Resonnance Spectrometers* (Ellis Horwood Ltd. and PWN Scientific Publishers, New York, 1989).

36. E. M. Chudnovski, Phys. Rev. B **40**, 2946 (1989).

37. L. D. Landau and M Lifshitz, *Theory of Elasticity* (Pergamon. New York, 1970).

38. A. Mychielski, P. Dzwonkowski, B. Kowalski, B. A. Orlowski, . Dobrowolska, M. Arciszewska, W. Dobrowolski, and . M. Baranowski, J Phys. C: Solid State Phys. 19, 3605 (1986).

39. Yu I. Ravick, B. S. Efimova, and V. I. Tamarchenko, Phys. Stat. Sol. (b) **43**, 453 (1971).

40. R. Granger, A. Lasbley, C. M. Pelletier and S. Rolland, J. de Phys. 46, 1185 (1985).

41. B. A. Lombos, C. Fau, M. Averous, and J. M. Lacroix, Sol. Stat. Comm. **72**, 909 (1989).

42. B.A. Lombos, M. Averous, C. Fau, R. Le Van Mao, P. Silvestre and A. Jean, E-MRS Spring Meeting, Strasbourg (1990).

43. D. Côte, J. P. Dodelet, B. A. Lombos, and J. I. Dickson, J. Electrochem. Soc. 9, 1925 (1986).

44. B. A. Lombos, D. Côte, J. P. Dodelet, M. F. Lawrence, and J. I. Dickson, J. Crystal Growth 79, 455 (1986).

45. B. A. Lombos, J. P. Dodelet, A. Jean, T. Bretagnon, R. Le Van Mao, and D. Cossement, 1st Int. onf. on Epitaxial Crys. Growth EPI-1, 1990.

46. F. hasegawa, M. Onomura, C. Mogi, and Y. Nannichi, Sol. Stat. Electron. 31, 223 (1988).

47 M. C. Chen, D. V. Lang, W. C. Dantremont-Smith, A. M. Sergent, and J. P. harbison, Appl. Phys. lett. **44**, 790 (1984).

48. A. Yahata, and M. Nakajima, Jpn J. Appl. Phys. 23, L313 (1984).

49. W. Walukiewicz, L. Lagowski, L. Jastrzebski, M. Lichtensteiger, and H. C. Gatos, J. Appl. Phys. 50, 899 (1979).

50. R. Hackam, and P. Harrop, IEEE Trans. on Electron. Dev. **ED-19**, 1231 (1972).

51. J. D. Levine, J. Appl. Phys. **42**, 3991 (1971).

52. C. R. Crowell, Sol. Stat. Electron. **9**, 1035 (1966).

53. C. R. Crowell, and V. L. Rideout, Sol. Stat. Electron. **12**, 89 (1969)

54. B A Lombos, Can J Chem. 63. 1666 (1985).

55. W. Shockley, *Electrons and Holes in Semiconductors* (D. Van No[illegible], Princeton, 1950).

56. A. Micea, A. Mitonneau, L. Holland, and A. Briere, Appl. Phy[illegible] 11, 153 (1976).

APPENDIX A

PROCEDURE USED FOR THE FABRICATION OF OHMIC CONTACTS ON PbGdTe

At first, the sample is cut in parallelepiped shape using a mechanical saw. The dimension is varied since it depends on the monocristalline region of the bulk crytal. The sample is then polished using a felt spinning dish and a solution of brome-methanol for about few minutes, following by a rinse in methanol and deonized water. t is subsequently put in an ultra-sonic bath to remove eventual residual dust resulting from the polishing step.

The etching is done using a solution of KOH:H_2O_2:Ethylen Glycol (5:1:5) for about 20 to 30 minutes at room temperature. The sample is then rinsed in a bath of ethanol and subsequently in deonized water. Once the sample is clean, a thin layer of gold is deposited electrolytically. To do so, a small amount of golden cyanide is dropped on the surface of the sample where the ohmic contact should be made. As the drop is gathered, An electrode is sticked on its outer surface, without touching the sample. By properly biasing the sample and the electrode, the resulting electric current will induced a formation of a layer of gold on the surface of the crystal. The thickness of this layer can be increased by repeating the same operation for the same plot several times.

A low emf alloy is used as solder to bond contact to a golden wire. The elements used for the alloy are cadmium (9 %), tin (16 %), le[illegible] %) and bismuth (53 %). This solder alloy has a point of fusion [illegible] celsius and therefore can be easily applied without altering the [illegible] surface of the material. The flux for this solder alloy is obt[illegible] mixing 30 g of zinc chloride and 4 g of ammonium chloride with [illegible] of water.

The two ends of the parallelepiped are covered by an ohmic [illegible] The distance between the potential contacts (A,B) and (C,[illegible] typically from 1 cm to 2 cm. I-V measurements are made to ensure [illegible] the contacts remain ohmic over the temperature range of interest

APPENDIX B

PROCEDURE USED FOR OPERATING THE CRYOSTAT

The cryostat has a helium circulation system which allow to cover the temperature range from 4.2° K to 300° K (eventually lower temperature can be reached using an helium pump). The figure B.1 shows a schematic diagram of the cryostat. A diffusion pump is been used to create a vacuum to isolate the liquid nitrogen chamber from the outer wall, and an intermediary vacuum between the liquid nitrogen chamber and the liquid helium chamber. The same diffusion pump is also been used to evacuate the air in the helium chamber and the cylindrical enclosure which receives the sample holder prior to normal experiment. The last operation is important since helium gas is collected at the output to be recompressed later. An admission valve, usually opened, allows a connection between the liquid nitrogen chamber and the sample chamber. A helium flow can than circulate from the helium chamber directly to the sample chamber in order to reach quickly the temperature of 4.2° K. Pressure gauges provide feedbacks for the control of the internal pressures at different points in the helium circuit. The temperature sensors consist of a platinum resistor mounted on the sample holder and a carbon resistor mounted on the edge of the sample chamber. This set-up allows a temperature regulation under 50° K with a precision about 1° K. The cryostat is placed between two electro-magnets which allow a field up to 0.85 tesla. The current generator for the magnets is controlled by computer, so the field can be remotely swept or inverted.

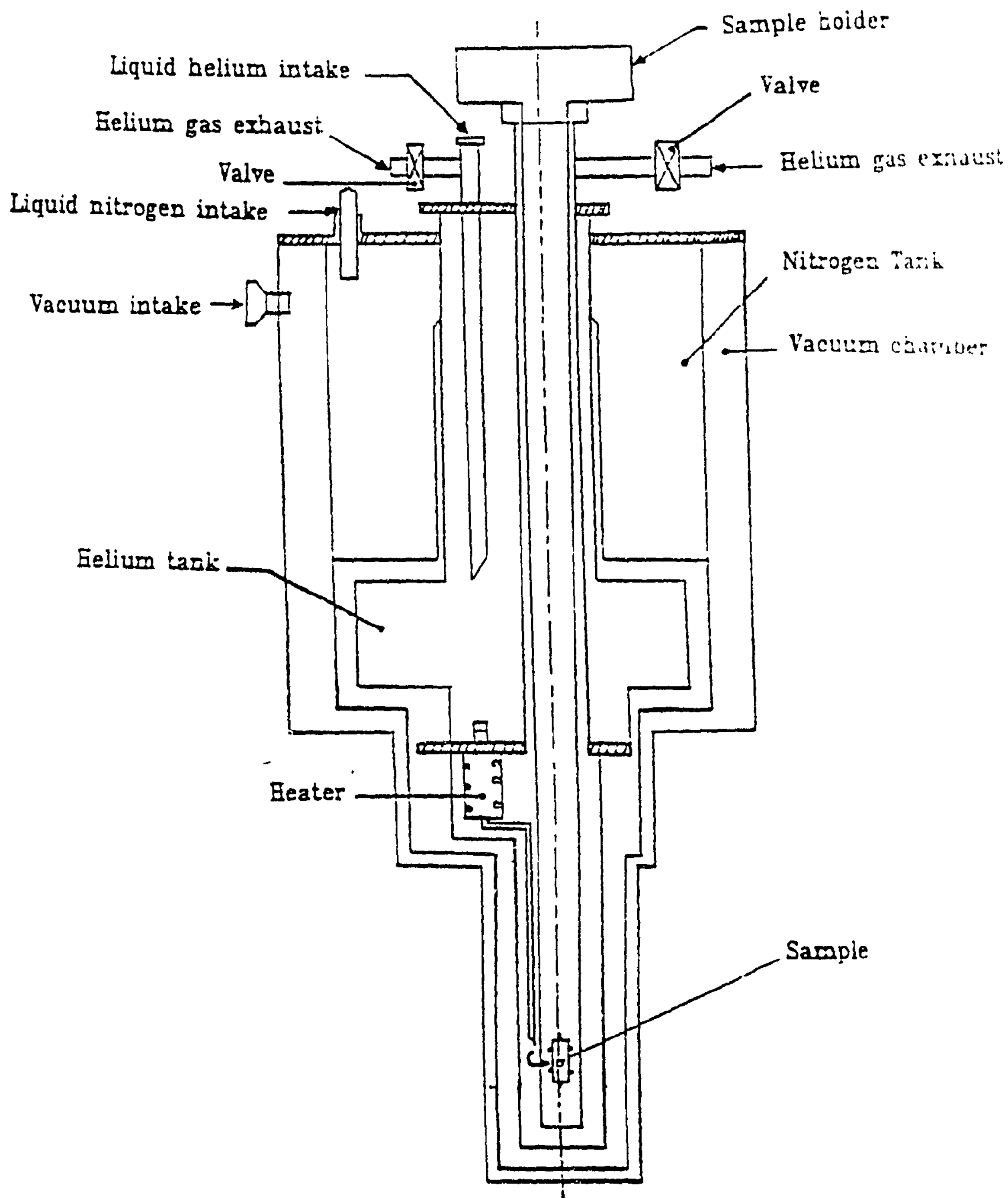

Figure B.1 Schematic diagram of the cryostat.

To reach the temperature of liquid helium from room temperature, the cryostat has to be cooled gradually. At first, the liquid nitrogen chamber is filled. Then, the sample chamber and the liquid helium chamber are filled with gaseous helium at low pressure in order to ease thermal exchanges. When the temperature in the sample chamber reaches around 170° K, liquid helium is poured in. By adjusting the pressure valves, one can maintain a continuous flow of the liquid through the sample chamber and, thereby, bring the temperature of the sample to 4.2° K. The hole operation requires approximately 7 to 8 hours. In the temperature range from 4.2° K to 30° K, the heat source for the temperature regulation comes from a resistance mounted in the sample holder. Over 30° K, all pressure valves are opened to avoid pressure build-up from evaporation of helium, the sample is then warmed up by inertia. The system takes more than 24 hours to reach room temperature. Meanwhile, the data acquisition system continues to take periodic readings and stores computed results.